

Exploring AGN and star formation activity of massive galaxies at cosmic noon

Jonathan Florez,¹★ Shardha Jogee,¹ Sydney Sherman,¹ Matthew L. Stevans,¹ Steven L. Finkelstein,¹ Casey Papovich,² Lalitwadee Kawinwanichakij,^{2,3} Robin Ciardullo,^{4,5} Caryl Gronwall,^{4,5} C. Megan Urry,^{6,7} Allison Kirkpatrick,⁸ Stephanie M. LaMassa,⁹ Tonima Tasnim Ananna¹⁰ and Isak Wold¹¹

¹Department of Astronomy, University of Texas at Austin, Austin, TX 78712, USA

²Department of Physics and Astronomy, Texas A&M University, College Station, TX 77843, USA

³Kavli Institute for the Physics and Mathematics of the Universe (Kavli IPMU, WPI), The University of Tokyo, Kashiwa 277-8583, Japan

⁴Department of Astronomy and Astrophysics, The Pennsylvania State University, University Park, PA 16802, USA

⁵The Institute for Gravitation and the Cosmos, The Pennsylvania State University, University Park, PA 16802, USA

⁶Yale Center for Astronomy & Astrophysics, New Haven, CT 06520, USA

⁷Department of Physics, Yale University, PO BOX 201820, New Haven, CT 06520, USA

⁸Department of Physics & Astronomy, University of Kansas, Lawrence, KS 66045, USA

⁹Space Telescope Science Institute, 3700 San Martin Dr, Baltimore, MD 21218, USA

¹⁰Department of Physics & Astronomy, Dartmouth College, 6127 Wilder Laboratory, Hanover, NH 03755, USA

¹¹NASA Goddard Space Flight Center, Greenbelt, MD 20771, USA

Accepted 2020 July 22. Received 2020 July 9; in original form 2020 March 16

ABSTRACT

We investigate the relation between active galactic nucleus (AGN) and star formation (SF) activity at $0.5 < z < 3$ by analysing 898 galaxies with X-ray luminous AGNs ($L_X > 10^{44}$ erg s^{−1}) and a large comparison sample of $\sim 320\,000$ galaxies without X-ray luminous AGNs. Our samples are selected from a large (11.8 deg²) area in Stripe 82 that has multiwavelength (X-ray to far-IR) data. The enormous comoving volume (~ 0.3 Gpc³) at $0.5 < z < 3$ minimizes the effects of cosmic variance and captures a large number of massive galaxies ($\sim 30\,000$ galaxies with $M_* > 10^{11} M_\odot$) and X-ray luminous AGNs. While many galaxy studies discard AGN hosts, we fit the SED of galaxies with and without X-ray luminous AGNs with Code Investigating GALaxy Emission and include AGN emission templates. We find that without this inclusion, stellar masses and star formation rates (SFRs) in AGN host galaxies can be overestimated, on average, by factors of up to ~ 5 and ~ 10 , respectively. The average SFR of galaxies with X-ray luminous AGNs is higher by a factor of ~ 3 – 10 compared to galaxies without X-ray luminous AGNs at fixed stellar mass and redshift, suggesting that high SFRs and high AGN X-ray luminosities may be fuelled by common mechanisms. The vast majority (> 95 per cent) of galaxies with X-ray luminous AGNs at $z = 0.5$ – 3 do not show quenched SF: this suggests that if AGN feedback quenches SF, the associated quenching process takes a significant time to act and the quenched phase sets in after the highly luminous phases of AGN activity.

Key words: galaxies: evolution – galaxies: general – quasars: general – galaxies: star formation.

1 INTRODUCTION

The epoch of $z \sim 1$ – 3 (when the universe was only ~ 2 – 6 Gyr old, corresponding to ~ 15 per cent to 50 per cent of cosmic history) is one of the most important and active epochs of galaxy formation. During this period, star formation (SF) and active galactic nuclei (AGNs) activity in galaxies peaked, massive clusters collapsed into existence, and galaxies underwent significant growth. Although SF and AGN activity both peaked during this epoch, it is unclear how the two processes are related. Observations show that the cosmic star formation rate (SFR) density and black hole accretion rate density peak at around $z \sim 2$ and decrease rapidly down to

$z \sim 0$ (Dickinson et al. 2003; Babić et al. 2007; Hopkins, Richards & Hernquist 2007; Wilkins, Trentham & Hopkins 2008; Jogee et al. 2009; Rigby et al. 2011; Delvecchio et al. 2014; Madau & Dickinson 2014). Furthermore, it is well known that the central black hole mass of galaxies correlates with the host galaxy bulge mass (Magorrian et al. 1998; McLure & Dunlop 2002) and bulge velocity dispersion (Ferrarese & Merritt 2000; Gebhardt et al. 2000; Kormendy & Ho 2013). These relationships have led to suggestions that the growth of black holes and galaxies may be closely intertwined, but the issue of coevolution is the subject of debate (e.g. Jahnke & Macciò 2011; Kormendy & Ho 2013).

AGN activity, which is a direct result of gas accreting on to a host galaxy’s central black hole, has often been proposed as a mechanism that can reduce or suppress SF activity, as radiation, winds, and jets expel gas or heat it enough to prevent it from forming stars.

* E-mail: jflorez06@utexas.edu

Different forms of AGN feedback impact their host galaxies in different ways. AGN feedback from radiation and winds from the accretion disc can heat or expel galactic gas on different physical scales (e.g. Hambrick et al. 2011; Fabian 2012; Vogelsberger et al. 2013; Choi et al. 2015; Roos et al. 2015; Hopkins et al. 2016; Bieri et al. 2017). Jets from AGNs are thought to play a large role in heating the intracluster medium (ICM) in clusters of galaxies, thus preventing gas from cooling and accreting on to galaxies and ultimately halting future episodes of star formation (e.g. Peterson & Fabian 2006; McNamara & Nulsen 2007; Somerville et al. 2008; Cattaneo et al. 2009; Fabian 2012; Heckman & Best 2014; Davé et al. 2019). In numerical simulations, some source of heating, such as AGN feedback, is thought to be crucial in solving the ‘overcooling’ problem in galaxy formation, where in absence of feedback, the gas inside dark matter haloes cools to form galaxies with mass functions resembling those of the dark matter haloes (White & Rees 1978; Somerville & Davé 2015; Naab & Ostriker 2017).

While AGN activity has been linked to a potential suppression of SF as described above, there are phases of galaxy evolution where AGN and SF activity coexist. A so-called AGN–SF connection has been claimed at $z < 0.1$ (Sanders et al. 1988; Mahoro, Pović & Nkundabakura 2017). This connection, however, is currently a topic of debate as other studies (e.g. Leslie et al. 2016) claim to find AGN activity associated with depressed SF activity at $z < 0.1$. Any potential connection between AGN and SF activity may be due, at least in part, to gas fuelling both the circumnuclear SF activity and AGN activity when the angular momentum problem can be overcome (e.g. Jogee 2006, and references therein), as is the case in gas-rich mergers (Hopkins et al. 2008). At higher redshifts, the AGN–SF connection is less well studied. Some studies have claimed $1 < z < 3$ galaxies with X-ray luminous AGNs, where X-ray emission is measured in the hard band (typically at 2–10 keV) or ultra-hard band (at 14–195 keV), have enhanced SFRs compared to galaxies without X-ray luminous AGNs and/or that X-ray luminous AGNs are preferentially found in star-forming galaxies out to $z \sim 2$ (Santini et al. 2012; Rosario et al. 2013; Shimizu et al. 2017; Masoura et al. 2018), while other studies (e.g. Shimizu et al. 2015) have claimed that galaxies with X-ray luminous AGNs have decreased SFRs compared to galaxies without luminous AGNs.

The goal of this work is to explore the general connections, if any, between AGN and SF activity in galaxies at early cosmic times. As outlined above, the relationship between AGN and SF activity might be expected to depend on the evolutionary phase of a galaxy and the AGN activity cycle. It is possible that early-on, X-ray luminous AGN and SF activity coexist when large gas inflows on different physical scales fuel both types of activity. At later times, the AGN feedback phase may start if AGN-driven radiation, winds, and jets eject or heat galactic gas on different scales. Our study aims to explore the relation between AGN and SF activity, and to constrain the relative importance and time-scales of these different evolutionary phases.

The processes that regulate SF and AGN activity are important for our understanding of galaxy evolution as they are intimately tied to the growth of galaxies. Observations have confirmed the existence of massive quenched galaxies up to $z \sim 4$ (Kriek et al. 2006; Baldry et al. 2012; Muzzin et al. 2013; Stefanon et al. 2013; Fang et al. 2018; Sherman et al. 2020; Glazebrook et al. 2017; Stevens et al. 2020), suggesting that quenching mechanisms can efficiently suppress SF in galaxies at early cosmic times. It is unclear, however, what role (if any) AGN feedback plays in the quenching of massive galaxies. Simulations, such as Illustris (Wellons et al. 2015) and IllustrisTNG (Naiman et al. 2018; Nelson et al. 2018;

Springel et al. 2018), largely implement AGN and stellar feedback as the main quenching mechanisms for massive galaxies in their simulations. However, these simulations struggle to produce massive quenched galaxies by $z \sim 3$. We aim to explore the properties of massive, quiescent galaxies with and without X-ray luminous AGNs in order to further constrain the processes that quench star formation.

Studying the SF activity of galaxies with X-ray luminous AGNs can be rather complicated, as the emission from an AGN can dominate the galaxy spectral energy distribution (SED) at ultraviolet (UV), optical, mid-IR, and far-IR wavelengths, thus making it difficult to disentangle the emission between AGNs and star-forming processes in SED fitting. For this reason, many studies that explore the global stellar mass-SF main sequence of galaxies explicitly remove or ignore the contribution from galaxies with X-ray luminous AGNs (Speagle et al. 2014). Although difficult, several studies have attempted to compare the star-forming properties of galaxies with X-ray luminous AGNs to galaxies without X-ray luminous AGNs, with X-ray emission measured in the hard band (at 2–10 keV) (Masoura et al. 2018) and the ultra-hard band (at 14–195 keV) (Shimizu et al. 2017), and find that galaxies with X-ray luminous AGNs tend to have enhanced SFRs with respect to galaxies without X-ray luminous AGNs. The work presented in this paper will utilize a control sample of galaxies without X-ray luminous AGNs that is larger than the control samples presented in the aforementioned studies and will use the same SED fitting code to measure galaxy properties for galaxies with and without X-ray luminous AGNs.

For this study, we create a sample of galaxies with X-ray luminous AGNs, where X-ray emission is measured in the full band of Stripe 82X at 0.5–10 keV, and a sample of galaxies without X-ray luminous AGNs using the same photometric data and perform SED fits of both samples using Code Investigating GALaxy Emission (CIGALE) (Boquien et al. 2019; Ciesla et al. 2015; Noll et al. 2009) which is capable of disentangling the emission from AGNs and star-forming processes. This allows us to measure and compare the star-forming properties of both samples in the same self-consistent way, unlike many other studies. We select our samples from a very large 11.8 deg² field where the Stripe 82X X-ray survey (LaMassa et al. 2016) and the Spitzer-HETDEX Exploratory Large Area (SHELA) IRAC survey overlap Papovich et al. (2016). Our samples have extensive multiwavelength coverage (e.g. X-ray, UV, optical, near-to-mid-IR, and some far-IR/submillimetre) over the 11.8 deg² field, which corresponds to a very large comoving volume of ~ 0.3 Gpc³ at $z = 0.5$ – 3 . Such a large comoving volume minimizes the effects of cosmic variance and captures a large sample of rare massive galaxies ($\sim 30\,000$ galaxies with $M_* > 10^{11} M_\odot$) and X-ray luminous AGNs (~ 700 objects with $L_X > 10^{44}$ erg s^{−1}), allowing us to provide some of the strongest constraints to-date on the relation between AGN and SF activity at $z \sim 1$ – 3 .

This paper is organized as follows. In Section 2, we discuss the data we use to select and create our samples of galaxies with and without X-ray luminous AGNs. In Section 3, we describe the SED fitting method and tests we use to obtain galaxy properties, such as stellar mass and SFR. In Section 4, we discuss the stellar mass and SFR distributions of our samples. In Section 5.1, we compare the stellar mass–SFR relation of galaxies with and without X-ray luminous AGNs. In Section 5.2, we present the fraction and properties of quenched galaxies as a function of mass and redshift. We discuss our findings in Section 6, and in Section 7 we summarize our results. Throughout this paper, we assume $H_0 = 70$ km s^{−1} Mpc^{−1}, $\Omega_M = 0.3$, and $\Omega_\Lambda = 0.7$.

2 DATA AND SAMPLE SELECTION

The goal of this work is to estimate and compare the star-forming properties of galaxies with and without X-ray luminous AGNs at $z = 0.5–3$. To accomplish this, we utilize the large-area, multiwavelength data available in the SHELA/HETDEX footprint, which consists of five photometric datasets: Dark Energy Camera (DECam) u, g, r, i, z (Wold et al. 2019), NEWFIRM K_S (Stevens et al. submitted), *Spitzer*-IRAC 3.6 and 4.5 μm (Papovich et al. 2016), *Herschel*-SPIRE far-IR/submillimeter (HerS, Viero et al. 2014), and Stripe 82X X-ray (LaMassa et al. 2016). We also utilize available J - and K_S -band data from the VISTA-CFHT Stripe 82 (VICS82) Near-Infrared Survey (Geach et al. 2017) and mid-IR photometry from the WISE survey (Wright et al. 2010) to supplement this work. In the near future, optical integral-field spectroscopy between 3500 and 5000 \AA of this region will be available from the Hobby Eberly Telescope Dark Energy Experiment (Hill & HETDEX Consortium 2016).

2.1 NEWFIRM K -band selected catalogue

For the analysis presented in this paper, we use photometry from a NEWFIRM K_S -band selected catalogue (Stevens et al. submitted) that includes DECam u, g, r, i, z as well as IRAC 3.6 and 4.5 μm photometry spanning an area of 17.5 deg^2 across the SHELA field. The catalogue is created using an approach similar to that in Wold et al. (2019) and described in detail in Stevens et al. (submitted). In summary, they use Source Extractor (SEXTRACTOR; Bertin & Arnouts 1996) to identify sources in their K_S -band images and report a 5σ depth of ~ 22.4 AB mag inside fixed 2 arcsec diameter apertures. The K_S -band fluxes that we use for the analysis presented here are the Kron aperture fluxes from SEXTRACTOR (e.g. FLUX_AUTO). Quality flags in the catalogue allow us to exclude objects with saturated, truncated, or corrupted pixels as well as regions in close proximity to saturated stars from our analysis. The DECam and IRAC magnitudes are derived through forced photometry of NEWFIRM K_S selected sources using the *Tractor* image modelling code (see Lang, Hogg & Mykytyn 2016, for description of code). The *Tractor* code uses the source positions and surface brightness profiles of higher resolution bands to model and derive fluxes for remaining lower resolution bands. This allows the catalogue to include individual fluxes for potentially blended sources in IRAC. These debleded DECam and IRAC fluxes are used to create the K_S -selected DECam-NEWFIRM-IRAC catalogue that we use for this work.

2.2 Stripe 82X

Stripe 82X is an X-ray survey that covers 31.3 deg^2 of the SDSS Stripe 82 Legacy Survey (LaMassa et al. 2013a, b, 2016; Ananna et al. 2017). The original catalogue described in LaMassa et al. (2016) introduced the release of the *XMM-Newton* Announcement Opportunity 13 (‘AO13’) data and is combined with archival *XMM-Newton* and *Chandra* X-ray Observatory X-ray data (LaMassa et al. 2013b, a). We utilize two updated versions of the catalogue described in Ananna et al. (2017) (hereafter A17) and LaMassa et al. (2019) (hereafter LM19). The XMM AO13 footprint largely overlaps ($\sim 11.8 \text{ deg}^2$ overlap) with the SHELA field, whereas the archival *Chandra* and *XMM-Newton* data footprints hardly overlap with the SHELA field. For this reason, for our analysis we only consider XMM AO13 data from the Stripe 82X catalogue, which has a spatial resolution of ~ 6 arcsec (Strüder et al. 2001).

The A17 Stripe 82X catalogue provides multiwavelength counterpart matches to the X-ray sources by crossmatching to the

SDSS coadded catalogues of Fliri & Trujillo (2016) and includes IRAC photometry (Papovich et al. 2016; Timlin et al. 2016) in the crossmatching as well. The A17 catalogue also provides photometric redshifts for every source in the catalogue as well as quality flags that indicate the reliability of the match. A description of how photometric redshifts are obtained for the sample can be found in A17. The photometric redshifts (z_{phot}) when compared to the available spectroscopic redshifts (z_{spec}) have a scatter of $|\Delta(z)|/(1+z) \sim 0.06$ where $\Delta(z) = (z_{\text{phot}} - z_{\text{spec}})$ and a ~ 14 per cent outlier fraction, where outliers are defined as objects with $|\Delta(z)|/(1+z_{\text{spec}}) > 0.15$. We use the A17 catalogue to obtain full X-ray fluxes (0.5–10 keV), WISE counterpart fluxes, and redshifts for our sample of galaxies with X-ray luminous AGNs. We utilize the aforementioned LM19 catalogue to add additional spectroscopic redshifts to the sources in XMM AO13, which brings the spectroscopic redshift completeness for our sample of galaxies with X-ray luminous AGNs to ~ 75 per cent.

2.3 VICS82 and WISE supplemental data

A significant portion of the SHELA footprint overlaps with the VICS82 survey (Geach et al. 2017) and the WISE (Wright et al. 2010) mid-IR survey. The DECam-NEWFIRM-IRAC catalogue we utilize includes matches to VICS82 J - and K_S -band photometry. We make use of the VICS82 J - and K_S -band photometry in our analysis in order to better constrain the SED fit at near-IR wavelengths. We crossmatch sources in the DECam-NEWFIRM-IRAC catalogue to the AllWISE source catalogue (Wright et al. 2010) by considering any objects within 1.5 arcsec of the NEWFIRM source a match. We utilize the magnitude values from the profile-fitting photometry and only consider sources with $S/N > 2$ for this work. Due to the lower resolution of WISE photometry ($\sim 6–7$ arcsec for WISE-1–3, ~ 12 arcsec for WISE-4), we only consider objects a match for this work if the WISE source has no more than one NEWFIRM match within a 5 arcsec radius, thus avoiding blended sources. In addition, we apply flag quality cuts to make sure none of our WISE sources have image pixels in the measurement aperture that are confused with nearby sources, and/or contaminated by saturated or otherwise unusable pixels. WISE photometry, particularly in the WISE-3 (12 μm) and WISE-4 (22 μm) bands, is particularly useful for constraining the SED in the mid-IR wavelengths where emission from an AGN can contaminate the emitted light at 3–20 μm and dust emission from SF radiates at 8–1000 μm . As discussed in the following sections and illustrated in Fig. 1 and Table 1, we unfortunately find that only a small fraction of our sample has WISE-3 or WISE-4 photometry. Therefore, we mainly use WISE data to determine whether and how our results might change if mid-IR photometry is included (see Appendix).

2.4 Sample selection

In this section, we describe how we obtain our samples of galaxies with and without X-ray luminous AGNs. We start by selecting all sources in the K_S -selected DECam-NEWFIRM-IRAC catalogue that overlap the Stripe 82X AO13 footprint on the sky. From these sources, we create a sample of objects, which we refer to as S0-DECam-NEWFIRM-IRAC, that have a detection in the DECam u, g, r, i, z bands, a signal-to-noise (S/N) > 5 in the NEWFIRM K_S band, and $S/N > 2$ in the IRAC 3.6 and 4.5 μm bands. The reader can refer to the flowchart in Fig. 1 for an illustration of how the samples with and without X-ray luminous AGNs are selected from S0-DECam-NEWFIRM-IRAC (described in further detail below).

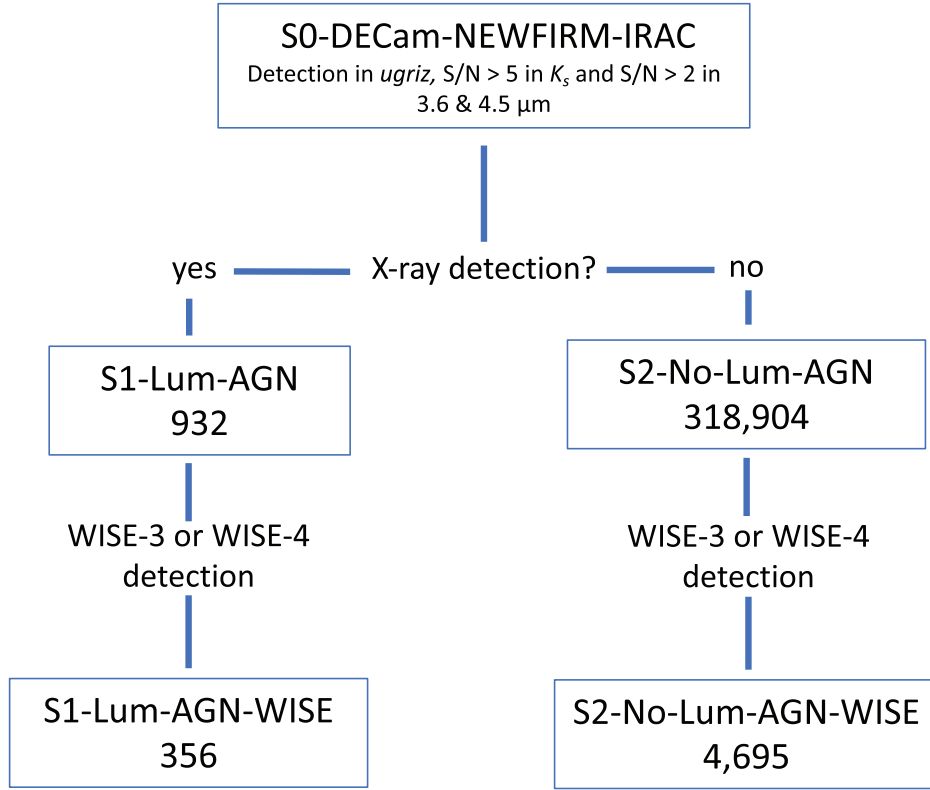


Figure 1. Flowchart that demonstrates how our samples are selected. We start with the DECam-NEWFIRM-IRAC catalogue and create a sample of sources that fit our selection criteria, which we refer to as S0-DECam-NEWFIRM-IRAC (see Sections 2.1 and 2.4). We then crossmatch S0-DECam-NEWFIRM-IRAC with the Stripe 82X catalogue via the MLE method and create samples with and without an X-ray match, which we refer to as S1-Lum-AGN (see Section 2.4.1) and S2-No-Lum-AGN (see Section 2.4.2), respectively. We then search for WISE detections in both S1-Lum-AGN and S2-No-Lum-AGN and create two more samples, which we refer to as S1-Lum-AGN-WISE and S2-No-Lum-AGN-WISE. The reader can refer to Table 1 for number of objects in each sample complete in X-ray luminosity and stellar mass. We note that although we have 932 sources with X-ray luminous AGNs in sample S1-Lum-AGN, only 898 of these are have a good SED fit with a reduced χ^2 of less than 5. We therefore only analyse these 898 sources in S1-Lum-AGN for this work.

2.4.1 Galaxies with X-ray luminous AGNs

In order to create a sample of X-ray selected AGNs, we crossmatch between XMM AO13 sources from the Stripe 82X catalogue and sources in S0-DECam-NEWFIRM-IRAC using the maximum likelihood estimator (MLE) method of Sutherland & Saunders (1992). The MLE method has been widely used to perform crossmatching between X-ray data and multiwavelength counterparts (see Brusa et al. 2010; LaMassa et al. 2016, 2013b; Ananna et al. 2017). We implement the same MLE methodology used in LaMassa et al. (2016). That is, we set our search radius to 7 arcsec and the background search radius to be between 10 and 45 arcsec. We use X-ray positional error values given in the LaMassa et al. (2016) catalogue and assume that the positional errors in the DECam-NEWFIRM-IRAC catalogue are negligible compared to those of the X-ray. The only difference in our method to that of LaMassa et al. (2016) is that we consider objects that have a reliability value (R in equation 2 of LaMassa et al. 2016) greater than 0.5 to be true matches, as any object with $R > 0.5$ is the most likely source inside the search radius to be the true counterpart. We only crossmatch to the K_s -band photometry in the DECam-NEWFIRM-IRAC catalogue as we are using a K_s -band selected catalogue for the analysis presented here.

Once we find a match between S0-DECam-NEWFIRM-IRAC and XMM AO13, we assign it a photometric or spectroscopic (if available) redshift from A17. We create the sample S1-Lum-AGN

from sources in S0-DECam-NEWFIRM-IRAC that have an X-ray match and $z = 0.5-3$. From this sample, we search in A17 for any sources that have a WISE detection and include those in our subsample S1-Lum-AGN-WISE. Out of 1356 unique XMM AO13 X-ray sources that fall in the SHELA footprint at $z = 0.5-3$, we find a total of 932 reliable matches in the DECam-NEWFIRM-IRAC catalogue. Of these, only 356 sources have a detection in either the WISE-3 or WISE-4 bands.

In Fig. 2, we show the full (0.5–10 keV) X-ray luminosity function of all sources in XMM AO13, those matched with S0-DECam-NEWFIRM-IRAC, and those that are matched with a WISE-3 or WISE-4 detection. Although we calculate the X-ray luminosity function here to show the effects of requiring photometric completeness and WISE photometry on our sample, we refer the reader to Ananna et al. (2019) for the latest evolving X-ray luminosity function which includes the effects of X-ray absorption and also includes data from multiple surveys in order to overcome the luminosity–redshift correlation in any one flux-limited survey. The X-ray luminosity function here is calculated using the $1/V_{\text{max}}$ method described in Schmidt (1968). In the $1/V_{\text{max}}$ method, the luminosity (or mass) function of a sample of galaxies is calculated by dividing the number of galaxies at a given luminosity (or mass) bin by the bin width times the differential comoving volume ΔV_C , where ΔV_C is the difference between the comoving volume (V_{max}) at a maximum redshift that a source of given luminosity (or mass) can probe and the comoving volume at the low edge of the redshift bin. This method tries to

Table 1. Total number of galaxies in each sample at a given redshift range.

Sample (a)	All z bins ($z = 0.5–3.0$) (b)	$z = 0.5–1.0$ (c)	$z = 1.0–1.5$ (d)	$z = 1.5–2.0$ (e)	$z = 2.0–3.0$ (f)
(1) S0-DECam-NEWFIRM-IRAC	319 836	156 978	91 193	22 753	48 912
(2) S1-Lum-AGN					
i.) Total number, N_{tot}	932	352	273	184	123
ii.) $L_X > L_{X,\text{lim}}$	386	147	136	71	32
iii.) $L_X > L_{X,\text{lim}}$ and $M_* > M_{*,95\%\text{lim}}$	258	131	83	30	14
(3) S1-Lum-AGN-WISE					
i.) Total number, N_{tot}	356	133	112	72	39
ii.) $L_X > L_{X,\text{lim}}$	193	75	64	35	19
iii.) $L_X > L_{X,\text{lim}}$ and $M_* > M_{*,95\%\text{lim}}$	130	71	37	12	10
(4) S2-No-Lum-AGN					
i.) Total number, N_{tot}	318 904	156 626	90 920	22 569	48 789
ii.) $M_* > M_{*,95\%\text{lim}}$	153 765	95 048	42 155	7991	8571
(5) S2-No-Lum-AGN-WISE					
i.) Total number, N_{tot}	4695	3487	903	116	189
ii.) $M_* > M_{*,95\%\text{lim}}$	4040	3353	836	98	132

Note: (1) The sample S0-DECam-NEWFIRM-IRAC contains galaxies that have a detection in the u, g, r, i, z bands, $S/N > 5$ in the K band, and $S/N > 2$ in the two IRAC bands, and overlap with the Stripe 82X survey (see flowchart in Fig. 1 for an illustration of how samples are selected). (2) The sample S1-Lum-AGN contains a subset of galaxies in S0-DECam-NEWFIRM-IRAC that have an X-ray luminous AGN. The total number of galaxies in the sample, as well as the number of galaxies with X-ray luminosities above the completeness limit ($L_X > L_{X,\text{lim}}$) and stellar masses above the 95 per cent stellar mass completeness limit ($M_* > M_{*,95\%\text{lim}}$) are shown. (3) The sample S1-Lum-AGN-WISE contains the much smaller subset of galaxies in S1-Lum-AGN that have matching WISE photometry. (4) The sample S2-No-Lum-AGN contains the subset of galaxies in S0-DECam-NEWFIRM-IRAC that do not contain an X-ray luminous AGN. (5) The sample S2-No-Lum-AGN-WISE contains the smaller subset of sources in S2-No-Lum-AGN that also have WISE photometry.

correct the luminosity (or mass) function for the fact that flux-limited observational surveys increasingly fail to detect faint sources at higher redshifts, and are therefore biased to produce an artificial drop in the number density of faint sources at higher redshifts. We note that the X-ray luminosity function drops by almost an order of magnitude for sources with WISE-3 counterparts above the X-ray completeness limit, and even more for sources with WISE-4 counterparts. This means that requiring a WISE-3 or WISE-4 detection would cause us to incompletely sample the X-ray luminosity function at $z = 0.5–3$. Furthermore, as shown in Fig. 1 and Table 1, our sample of X-ray luminous AGN (S1-Lum-AGN) would be reduced from 932 to 356 sources if we require WISE detections. Therefore, in order to better sample the X-ray luminosity function and prevent a drastic reduction in sample size, we do not use S1-Lum-AGN-WISE in our main analysis. However, in the Appendix, we perform tests on this sample to verify that the inclusion of WISE mid-IR data would not change the results of this work.

Table 1 shows the total number of sources (N_{tot}) in the full sample based on the DECam-NEWFIRM-IRAC catalogue (S0-DECam-NEWFIRM-IRAC), the sample of X-ray luminous AGNs (S1-Lum-AGN), and the subset of the latter sample with WISE detections (S1-Lum-AGN-WISE), as well as the number of sources above the X-ray completeness limit and stellar mass completeness limit for each sample. The X-ray luminosity completeness limit we use here is computed from the 80 per cent completeness full flux band limit of XMM AO13 ($F_X = 2.0 \times 10^{-14}$ erg s $^{-1}$ cm $^{-2}$), estimated from the flux area curves given in LaMassa et al. (2016). We take this flux limit and convert to a luminosity at the high end of each given redshift range to generate an 80 per cent luminosity completeness limit of $L_X = 10^{44.03}$ erg s $^{-1}$ at $z = 0.5–1$, $L_X = 10^{44.47}$ erg s $^{-1}$ at $z = 1–1.5$, $L_X = 10^{44.78}$ erg s $^{-1}$ at $z = 1.5–2$, and $L_X = 10^{45.21}$ erg s $^{-1}$ at $z = 2–3$. The source of X-ray emission for all galaxies in this sample should be entirely dominated by the respective AGN

component of each galaxy, given that we only analyse sources with $L_X > 10^{44}$ erg s $^{-1}$. AGN activity is the most likely mechanism in a galaxy capable of producing such high X-ray luminosities (Brandt & Alexander 2015).

As an additional test, we explore whether our selection of X-ray luminous AGNs using the X-ray energy band at 0.5–10 keV might lead us to pick low-luminosity AGNs with enhanced SF by comparing our study with other studies that use the more traditional X-ray hard band luminosities, at 2–10 keV, for selecting AGNs (Brandt & Hasinger 2005; Brandt & Alexander 2015; Masoura et al. 2018; LaMassa et al. 2019). These studies classify sources with hard X-ray band luminosities greater than $L(2–10 \text{ keV}) \sim 10^{42}$ erg s $^{-1}$ as sources hosting X-ray luminous AGNs, while galaxies without AGNs typically have hard X-ray emission below this threshold and an extremely small number of starburst galaxies may exceed this threshold, but not by much (Lehmer et al. 2008). We compute the rest-frame hard X-ray luminosity for each source as described in LaMassa et al. (2019) and find that all sources in our sample with X-ray full band (0.5–10 keV) luminosities above 10^{44} erg s $^{-1}$ have rest-frame X-ray hard band (2–10 keV) luminosities greater than $10^{43.5}$ erg s $^{-1}$, which is more than a magnitude greater than the $L(2–10 \text{ keV}) = 10^{42}$ erg s $^{-1}$ luminosity threshold used in the aforementioned studies. Therefore, we conclude it is unlikely that many of our X-ray luminous AGNs are actually low-luminosity AGNs with enhanced SF.

It is important to note here that our sample likely contains a large number of Type I AGNs (i.e. AGNs whose broad-line region is visible with respect to the observer) and a very small number of Type II AGNs (i.e. AGNs whose broad-line region is obscured with respect to the observer) as several studies (Burlon et al. 2011; LaMassa et al. 2016) find very few obscured AGNs with X-ray luminosities above 10^{44} erg s $^{-1}$. These obscured sources in Stripe 82X tend to be optically classified as ‘normal’ galaxies but are considered AGNs

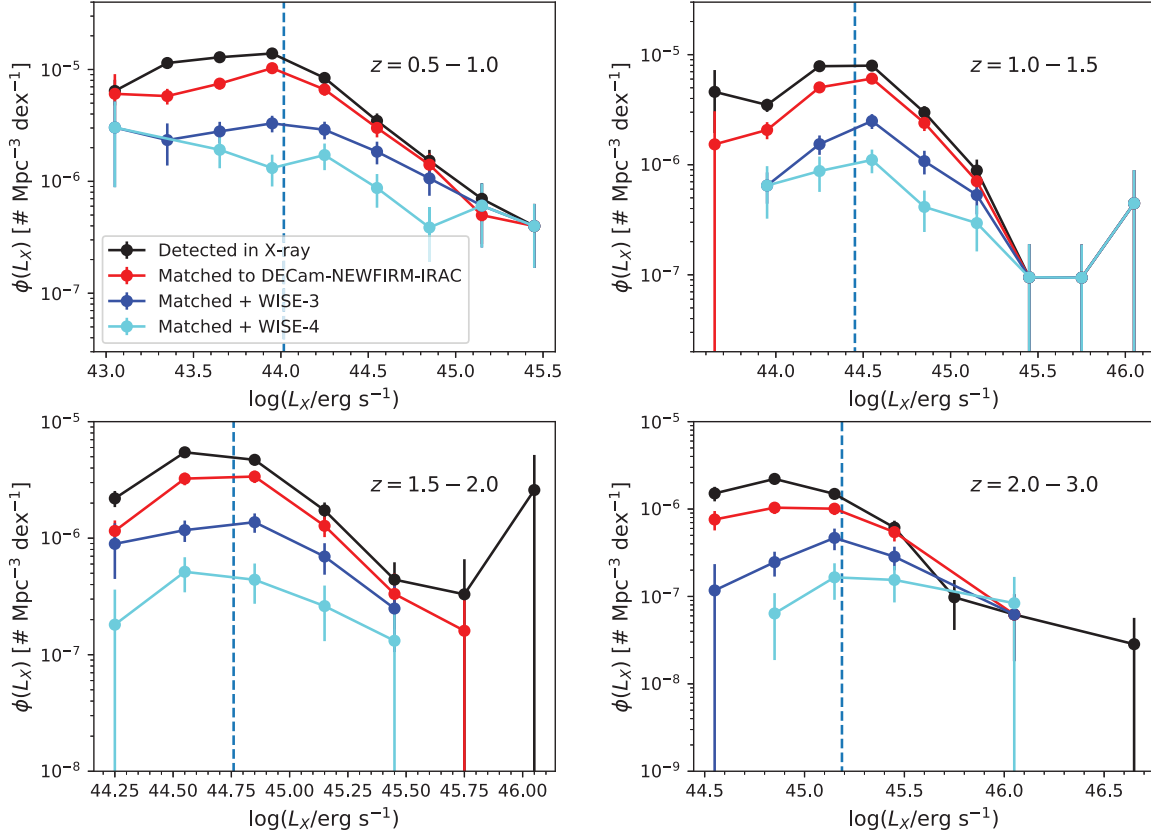


Figure 2. The full (0.5–10 keV) X-ray luminosity function of all XMM AO13 sources that fall in SHELA (black), those that have a reliable counterpart in the DECam-NEWFIRM-IRAC catalogue through crossmatching with the MLE method (red), matched sources with a WISE-3 detection (dark blue), and matched sources with a WISE-4 detection (light blue) in four different bins of redshift. The luminosity function here is computed using the V_{\max} method (see Section 2.4.1). The dashed line in each panel indicates the 80 per cent X-ray luminosity completeness limit, computed from the 80 per cent flux limit at the upper edge of each redshift bin.

because their X-ray luminosities exceed the 10^{42} erg s $^{-1}$ luminosity threshold, while quasars and broad-line sources can be found at all X-ray luminosities and make up the majority of sources with X-ray luminosities greater than 10^{44} erg s $^{-1}$. We therefore note that the results of the analysis presented in this paper do not extend to all populations of AGN types, and likely apply mostly to Type I AGNs (broad-line sources and quasars). While it is possible that we could also be missing obscured sources in our sample that are intrinsically X-ray luminous AGNs, we note that Powell et al. (2020) estimate how many additional X-ray luminous AGNs would be added to their high-luminosity sample ($L_X > 10^{44.5}$ erg s $^{-1}$, where L_X is the X-ray full band luminosity at 0.5–10 keV) if they corrected their luminosities for dust obscuration assuming a column density distribution matching that of XMM-XXL AGNs (Liu et al. 2016) and found that their sample would only increase by $\lesssim 4$ per cent. We therefore conclude that our sample of X-ray luminous AGNs is unlikely to be missing many luminous AGNs due to dust obscuration.

2.4.2 Galaxies without X-ray luminous AGNs

We create a sample of galaxies without X-ray luminous AGNs, which we refer to as S2-No-Lum-AGN, from sources in S0-DECam-NEWFIRM-IRAC that do not have an X-ray counterpart. We derive photometric redshifts for this sample using the EAZY-py photometric redshift SED fitting code (description of original EAZY code in

Brammer, van Dokkum & Coppi 2008) and keep all sources with $z_{\text{phot}} = 0.5\text{--}3$. EAZY-py fits a set of Flexible Stellar Population Synthesis (FSPS) templates (Conroy & Wechsler 2009; Conroy, Gunn & White 2009) that span a wide range of galaxy types (e.g. star forming, quiescent, dusty, etc.) in non-negative linear combination. The photometric redshift, z_{phot} , is determined from the combination of templates that have the lowest χ^2 value. To ensure we have a sample of galaxies that are all well fit by the EAZY-py templates, we implement a cut of $\chi^2 < 10$ on the entire sample. Comparison with the available SDSS spectroscopic redshifts reveal a 1σ scatter of $\Delta z/(1 + z_{\text{spec}}) = 0.037$. Although this comparison is only done for bright, low-redshift ($z < 1$) sources, Sherman et al. (2020) find a 1σ scatter of $\Delta z/(1 + z_{\text{spec}}) = 0.168$ for a sample of 16 bright $1.5 < z < 3.5$ galaxies with HETDEX spectroscopic redshifts using EAZY-py and the same photometry we use in this work, indicating fair agreement between the EAZY-py redshifts and spectroscopic redshifts. We explore the impact of uncertainty in redshifts on the SFRs of our sample of galaxies without X-ray luminous AGNs by shuffling the EAZY-py redshifts by 1σ . For the aforementioned case of $\sigma = 0.037$ (applicable to bright sources with $z < 1$), there is a scatter of $\sim 2\text{--}3$ when comparing the reshuffled SFRs to the original SFRs, but the average SFR remains the same. For the case of $1\sigma = 0.168$ (which applies for galaxies at $1.5 < z < 3.0$), we find that after shifting the photometric redshift of our galaxies at $z > 1.5$ by 1σ , the majority (> 90 per cent) of galaxies have reshuffled SFRs within 0.5 dex of the original SFR, while a small percentage (< 2 per cent) have

SFRs that shift by more than 1 dex. We therefore conclude that this photometric redshift uncertainty would not change the main results of this paper.

We create a subsample of objects in S2-No-Lum-AGN with a WISE-3 or WISE-4 counterpart, which we refer to as S2-No-Lum-AGN-WISE by crossmatching with the WISE catalogue. Similar to what is described for S1-Lum-AGN-WISE in the previous section, we do not include S2-No-Lum-AGN-WISE in our main analysis. Rather, in the Appendix, we perform tests on this sample S2-No-Lum-AGN-WISE to verify that the inclusion of WISE mid-IR data would not change the results of this work.

Our sample S2-No-Lum-AGN has a total of 318 904 sources. Of these, only 4695 have a WISE-3 or WISE-4 detection. The number of sources in S2-No-Lum-AGN and S2-No-Lum-AGN-WISE is also shown in Table 1, along with the number of sources above the stellar mass completeness limit at a given redshift range.

3 SED FITTING

In this section, we describe the SED fitting process that allows us to derive stellar masses and SFRs for our samples. One challenge that has persisted in the study of AGN host galaxies is determining the impact of AGN emission on the host galaxy’s SED and having the ability to accurately decompose the galaxy SED into stellar, dust, and AGN components. An AGN can have a significant effect on the light of the galaxy SED across a wide range of wavelengths, and the magnitude of the effect depends on the strength and phase of the AGN, and the orientation of the AGN with respect to the observer. Another challenge that persists in the study of AGNs is due to the wide variety of SED fitting codes. Many SED fitting codes do not include AGN emission templates in their code [e.g. EAZYpy (Brammer et al. 2008), MAGPHYS (da Cunha, Charlot & Elbaz 2008), iSEDfit (Moustakas et al. 2013), GalMc (Acquaviva, Gawiser & Guaita 2011), etc.], while others that do include AGN emission [e.g. AGNfitter (Calistro Rivera et al. 2016), SED3FIT (Berta et al. 2013), etc.] will often try to include an AGN component where none may exist, thus making such codes unsuitable for fitting samples of galaxies without X-ray luminous AGNs. This creates a further issue: many studies that measure and compare the properties of galaxies with luminous AGNs to galaxies without luminous AGNs do not estimate the properties of both populations in a self-consistent manner (Santini et al. 2012; Shimizu et al. 2015, 2017; Masoura et al. 2018).

In order to accurately and consistently estimate properties of galaxies with and without X-ray luminous AGNs, we perform SED fitting of both samples using the CIGALE (version 2018.0; Noll et al. 2009; Ciesla et al. 2015) SED fitting code. The CIGALE code offers several advantages over other SED fitting codes. First, CIGALE allows one to optionally include AGN emission templates in the SED fitting. This means one can quantify how the derived galaxy properties are affected by the inclusion or exclusion of AGN emission templates in the fit. More significantly, however, it allows us to derive stellar mass and SFR for galaxies with and without X-ray luminous AGNs accurately and consistently using the exact same code.

We fit a total of nine free parameters to the SED fit for our samples of galaxies with X-ray luminous AGNs: four parameters for the star formation history (SFH), one parameter for the dust attenuation, and four parameters for the AGN emission templates. For galaxies without X-ray luminous AGNs, we only fit five free parameters as we omit fitting the AGN emission templates for these galaxies. In our SED fitting of galaxies with X-ray luminous AGNs, we include the AGN emission models of Fritz, Franceschini & Hatziminaoglou (2006) for emission from the AGN accretion disc and dusty torus in the fit. For these AGN emission templates, we fit the AGN fraction

contamination, f_{AGN} , which is the total amount of light emitted at 8–1000 μm that is attributed to the AGN, the orientational angle of the AGN ($\Psi = 0^\circ$ for a type II AGN, $\Psi = 90^\circ$ for a type I AGN), the optical depth at 9.7 μm , and the ratio of the maximum to minimum radii of the dusty torus. For both samples of galaxies with and without X-ray luminous AGNs, we include models of dust emission attributed to SF (Dale et al. 2014), and the stellar populations of Bruzual & Charlot (2003). We assume attenuation of the galaxy SED by dust as described in Calzetti et al. (2000), a Chabrier initial mass function (IMF; Chabrier 2003), and a delayed exponential SFH with a constant burst/quench term described by the following equation:

$$\begin{aligned} \text{SFR}(t) &\propto t \times \exp(-t/\tau), \text{ when } t \leq t_{\text{trunc}} \\ \text{SFR}(t) &\propto r \times \text{SFR}(t = t_{\text{trunc}}), \text{ when } t > t_{\text{trunc}}, \end{aligned} \quad (1)$$

where r is the constant burst/quench term, defined as the ratio between $\text{SFR}(t)$ and $\text{SFR}(t = t_{\text{trunc}})$ at $t > t_{\text{trunc}}$, and t_{trunc} is the time at which the SFR experiences an instantaneous increase or decrease given by the burst/quench term r (see Ciesla et al. 2018, 2016, for description of SFH). Previous studies (e.g. Boselli et al. 2006; Fumagalli et al. 2011) have proposed using a delayed SFH which could undergo a strong decrease in SFR. Such an SFH would allow for more flexibility in modelling the recent SFH of quenched galaxies or starbursts (Ciesla et al. 2016, 2018). Ciesla, Elbaz & Fensch (2017) showed that this SFH provides a good estimate of the SFR on main-sequence galaxies, starbursts, and rapidly quenched systems at all redshifts. The SFRs we report here are the instantaneous SFRs given by this SFH, and thus, are obtained from equation (1) at $t = t_{\text{age}}$, where t_{age} is the presently observed age of the galaxy.

We make note here of the various factors that contribute to the dispersion of estimated SFRs. Work done by Buat et al. (2014) assesses the reliability of estimated SFRs from CIGALE for galaxies at $1 < z < 3$. They report full consistency between the instantaneous SFRs output by CIGALE, assuming different SFHs, to total SFRs estimated by empirical recipes using UV and FIR luminosities, suggesting the choice of SFH in CIGALE does not have a strong impact on the estimated SFR. Additionally, it is important to note that differences in the IMF and metallicity can affect the estimate of SFR. Buat et al. (2014) find that variation in the IMF changes the derived SFRs by a factor of up to ~ 0.17 dex, and variation in metallicity can change the derived SFRs by a factor of up to ~ 0.2 . All of these factors are important to consider when estimating and reporting SFRs for a given sample, however, we believe the choice of SFH, IMF, and metallicity for this study should not have a large impact on our results.

We perform our analysis with the Fritz et al. (2006) smooth dusty torus AGN emission templates because they are by far the most flexible AGN emission models available in CIGALE and cover a large range of parameters. However, we discuss here the implications of selecting the smooth dusty torus models of Fritz et al. (2006) over the clumpy dusty torus models that several other studies have investigated (Mullaney et al. 2011; Meléndez et al. 2014). Observations have provided evidence in favour of both clumpy (Tristram et al. 2007) and smooth (Ibar & Lira 2007) dusty toroidal distributions which are both often used in modelling the SED of X-ray luminous AGNs. Feltre et al. (2012) perform a comparison of both smooth and clumpy dust torus distributions widely used in the literature, comparing the Fritz et al. (2006) models, for a smooth dusty torus, to the Nenkova et al. (2008) models, for a clumpy dusty torus. They find that models with matched parameters between smooth and clumpy distributions do not produce similar SEDs and only a very limited number of random parameter combinations can produce seemingly identical SEDs for both distributions. Interestingly, they find that

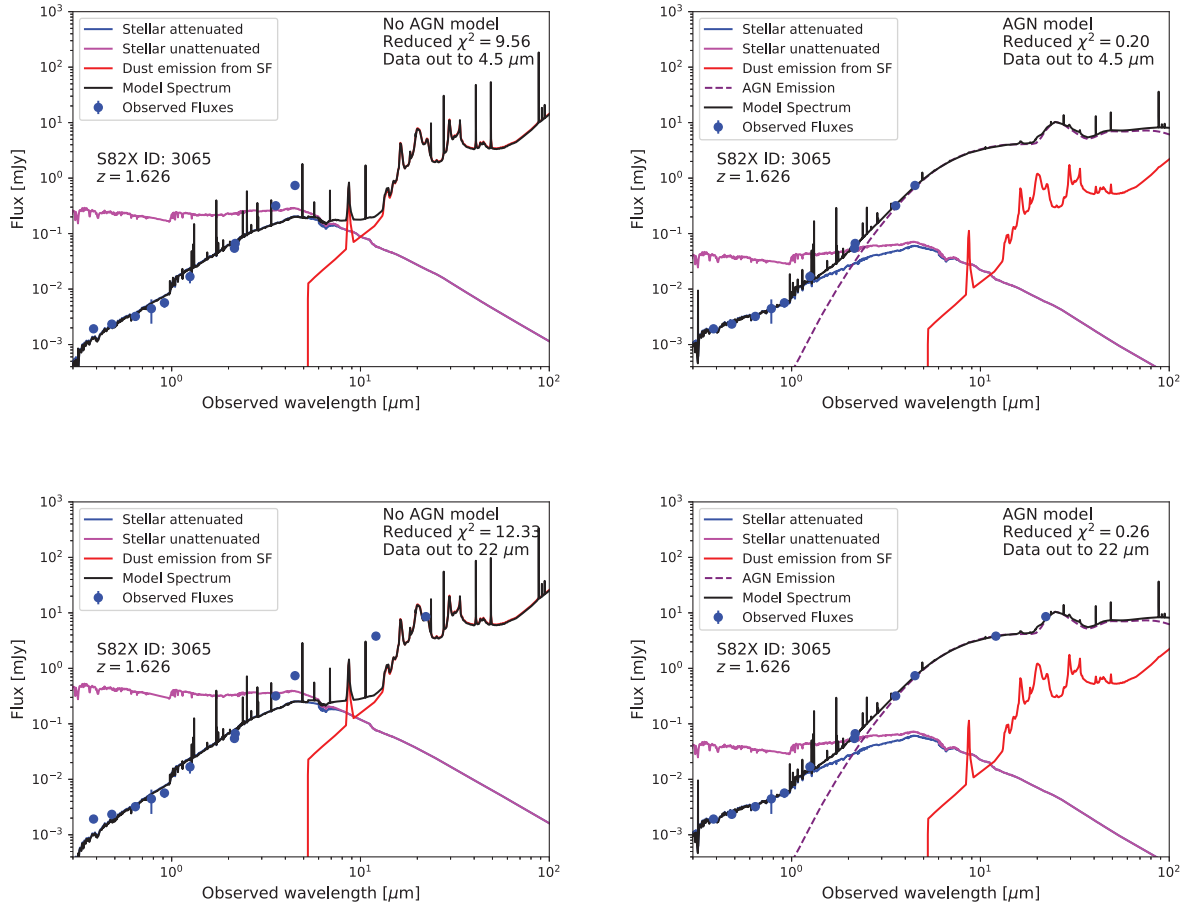


Figure 3. This figure compares model SED fits for a galaxy, whose redshift and Stripe 82X ID is displayed in each panel, with a type II X-ray luminous AGN in our samples S1-Lum-AGN (top two panels, with data coverage out to $4.5 \mu\text{m}$) and S1-Lum-AGN-WISE (bottom two panels with data coverage out to $22 \mu\text{m}$) for SED fits that do not include AGN emission (left) and include AGN emission (right). The final model SED fit (solid black line) with AGN emission (right) is made up of the attenuated stellar emission [blue; which is inferred from the unattenuated stellar emission (magenta)], the dust emission from dust heated by massive stars from recent SF (red), the combined AGN emission (purple) from the accretion disc (particularly important at UV+optical wavelengths) and the dusty torus (particularly important at the $3\text{--}1000 \mu\text{m}$ wavelength range). The best-fitting model SED without AGN emission (left) clearly cannot provide a good fit to the observed fluxes at wavelengths past $1 \mu\text{m}$, therefore, the AGN emission templates are needed in order to constrain all emission above $1 \mu\text{m}$. While WISE data at 12 and $22 \mu\text{m}$ can provide important constraints on the SED at longer wavelengths, a comparison of the top and bottom right panels of Fig. 3 shows that for the galaxy fitted here, the IRAC 3.6 and $4.5 \mu\text{m}$ photometry alone, without any WISE photometry, can provide important constraints on the SED fits with AGN emission templates.

most of the differences in the SEDs between these two published models are due to different dust chemical composition rather than dust morphology.

In terms of differences caused by dust morphology, Feltre et al. (2012) find that the clumpy AGN emission templates peak at slightly longer wavelengths, tend to have wider IR bumps, and steeper mid-IR slopes than the smooth dust models. It is possible that mean SFRs would be slightly lower when clumpy emission templates are applied as more emission at $8\text{--}1000 \mu\text{m}$ would be attributed to AGN activity, however, this would not be universal as the smooth templates could have wider IR bumps (within a matched parameter space than the clumpy templates).

3.1 Impact of AGN emission on SED fit and derived physical properties

It is especially important to include AGN emission in the SED fit of galaxies with X-ray luminous AGNs as it can have a drastic impact on the derived properties of the host galaxy, such as stellar mass and

SFR. In the UV+optical wavelength regime, a large portion of the emitted light of a luminous type I AGN (i.e. an AGN with the broad-line region visible to the observer) is attributed to the AGN accretion disc. In the case of type I and possibly type II AGNs (i.e. an AGN whose broad-line region is obscured with respect to the observer), at rest-frame wavelengths greater than $1 \mu\text{m}$, the SED of a galaxy with a luminous AGN is impacted by the AGN's dusty torus as the AGN's power-law flux drowns the polycyclic aromatic hydrocarbon (PAH) features in the SED. The CIGALE code includes the AGN emission of the accretion disc, as well as emission from the dusty torus in the SED fit, then carefully removes this emission from the derived SED when estimating the host galaxy properties.

In the top row of Fig. 3, we show as an example the SED of a galaxy with an X-ray luminous AGN before and after AGN emission is included in the fit for galaxies with data out to $4.5 \mu\text{m}$. Note that the AGN emission affects all emission above $1 \mu\text{m}$. The bottom row of Fig. 3 shows the same comparison, but this time also including WISE 12 and $22 \mu\text{m}$ photometry. While WISE data at 12 and $22 \mu\text{m}$ can provide important constraints on the SED at long wavelengths, a

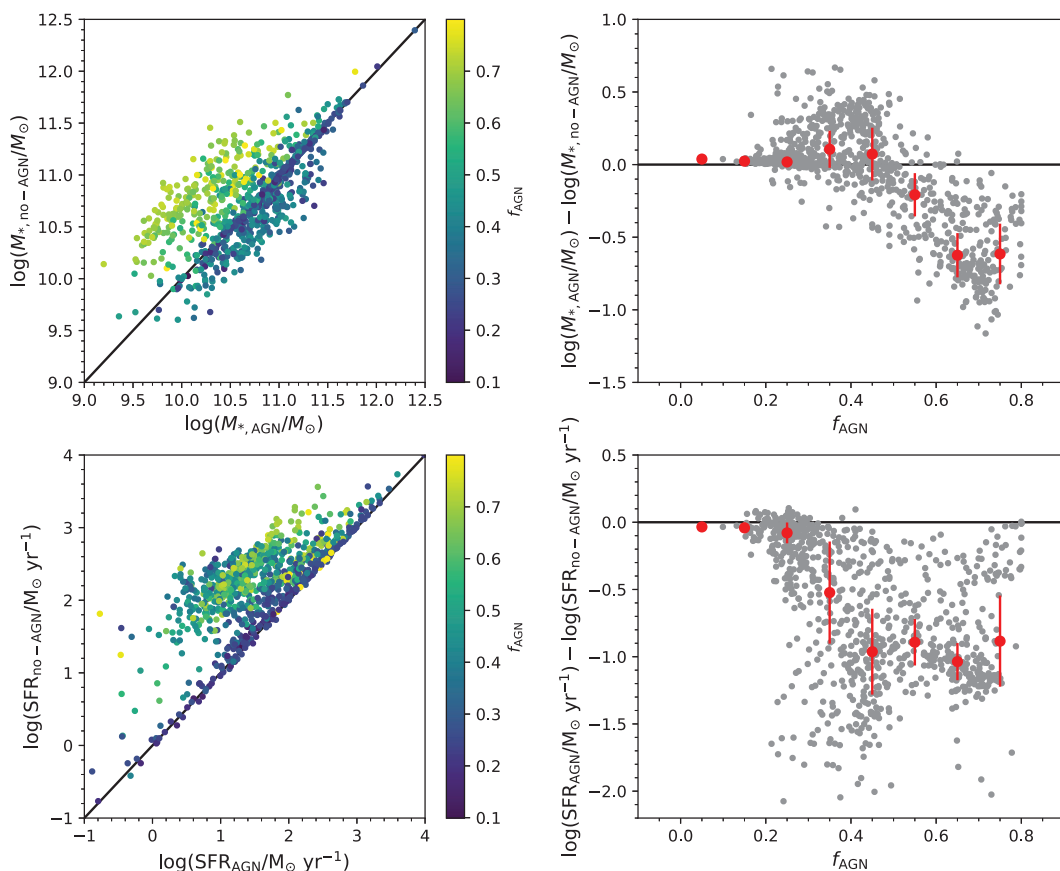


Figure 4. Left: Stellar mass and SFR estimates for our sample of galaxies with X-ray luminous AGNs (S1-Lum-AGN) when AGN emission is included in the SED fit (x-axis) versus when AGN emission is not included (y-axis). Points are coloured according to their fractional AGN contamination (f_{AGN}), defined as the fraction of light in the 8–1000 μm wavelength range that is contributed by the AGN. Right: Difference in log stellar mass and SFR as a function of the fractional AGN contamination. Also shown is the median (red circles) log difference of stellar mass and SFR with and without the AGN emission in the SED fit in four bins of f_{AGN} with the median absolute deviation shown as error bars. Note that for $f_{\text{AGN}} > 0.4$ stellar masses and star formation rates (SFRs) can be overestimated on average, by a factor of up to ~ 5 and ~ 10 , respectively, if AGN emission templates are not included in the SED fit.

comparison of the top and bottom right panels of Fig. 3 shows that in the galaxy fitted here, the IRAC 3.6 and 4.5 μm photometry alone, without any WISE photometry, can provide important constraints on the SED fits with AGN emission templates.

The inclusion of the AGN component can have a strong impact on the derived stellar masses and SFRs as the former will depend on whether the entire SED is dominated by a luminous AGN and the latter will depend on whether the UV and the near-to-far-IR light is attributed solely to stars and dust associated with SF or to a mix of stars, dust associated with SF, and AGNs. When including AGN emission in the model SED fit, the CIGALE code will estimate the fraction (f_{AGN}) of light in the 8–1000 μm wavelength range that is contributed by the AGN. In Fig. 4, we quantify the effect of not including an AGN component in the SED fitting using our sample of galaxies with X-ray luminous AGNs (S1-Lum-AGN), which have data from the UV band out to IRAC 4.5 μm , but no WISE data. Galaxies with $f_{\text{AGN}} < 0.4$ can have SFRs that are overestimated by a factor of up to 2, on average, and those with $f_{\text{AGN}} > 0.4$ can have SFRs overestimated by a factor of up to 10, on average, when AGN emission templates are not included in the SED fitting. In a few cases, the SFR can be overestimated by a factor ~ 100 when AGN emission templates are excluded from the SED fit. For this reason, we emphasize that SED fitting of galaxies with X-ray luminous AGNs should require AGN emission templates.

Fig. 4 also shows the impact on derived stellar masses. For $f_{\text{AGN}} > 0.4$, stellar masses can, on average, be overestimated by a factor of up to 5 when AGN emission templates are not included in the SED fit. This happens because without the AGN emission template, all of the light emission of the galaxy is assumed to come from stellar sources and dust as opposed to the AGN central engine. For galaxies with $f_{\text{AGN}} < 0.4$, stellar masses can be underestimated by a factor of up to 3 if AGN emission templates are not included in the SED fit. The underestimate of stellar masses in some of the galaxies with $f_{\text{AGN}} < 0.4$ happens because without the AGN emission templates, the AGN-boosted mid-IR luminosities of these galaxies will be fit by dusty stellar population templates instead of the AGN dusty torus templates. This in turn causes CIGALE to assume that the galaxy SED has a younger, dustier stellar population than it really does, thereby lowering the stellar masses estimates.

As mentioned earlier, the results shown in Fig. 4 are based on the sample of galaxies with X-ray luminous AGNs (S1-Lum-AGN) that have data from the UV band out to 4.5 μm , but no WISE data at 12 and 22 μm . We made the decision not to limit our analysis to only sources with WISE data as our sample size would be drastically reduced (see Fig. 1). Instead, we confirmed that not including the WISE data does not change the results in this paper by performing additional tests in the Appendix. Figs A1 and A2 in the Appendix show that the exclusion of WISE data does not change the results of

Fig. 4 and does not have a systematic effect on the derived stellar mass and SFR. This can in part be understood by the fact that in many galaxies, such as the one shown in Fig. 3, the SED fit is already constrained by the data just below 5 micron and remains unchanged with or without WISE photometry included in the fit.

We include AGN emission templates when we fit the samples (S1-Lum-AGN and S1-Lum-AGN-WISE) of galaxies hosting X-ray luminous AGNs. However, we do not include AGN emission templates in the SED fit of the sample (S2-No-Lum-AGN and S2-No-Lum-AGN-WISE) of galaxies without X-ray luminous AGNs because (a) it is computationally expensive to fit the AGN emission models to $>100,000$ galaxies and (b) when we do include the AGN emission in the SED fit of a small subsample of galaxies in S2-No-Lum-AGN-WISE we find that f_{AGN} is extremely low (<0.05) for 90 per cent of the sample, moderately low (<0.2) for 8 per cent of the sample, and that there is no systematic change in the derived SFRs.

4 DERIVED STELLAR MASS AND SFR OF SAMPLE GALAXIES

We discuss in the following subsections the stellar mass completeness, stellar mass function (SMF) (Section 4.1), and SFR distributions (Section 4.2) of our sample of galaxies with (S1-Lum-AGN) and without (S2-No-Lum-AGN) X-ray luminous AGNs.

4.1 Distribution of stellar masses

To estimate stellar mass completeness for each sample, we follow the procedure described in Pozzetti et al. (2010) and Davidzon et al. (2013). As per this method, we assume that the mass completeness limit of a survey can be estimated from the mass of the least massive galaxy that can be detected in a given bandpass with a magnitude equal to the magnitude limit of the survey in that bandpass. At each redshift, we select a representative sample from the faintest 20 per cent of galaxies and scale their stellar mass, $\log(M_*)$, using the following equation:

$$\log(M_{*,m=m_{\text{lim}}}) = \log(M_*) + 0.4(m - m_{\text{lim}}) \quad (2)$$

Here, m is the measured AB magnitude, and m_{lim} is the AB magnitude limit of the survey in a given bandpass. After scaling the stellar masses of the faintest 20 per cent of objects, we take the 95th percentile of the scaled mass distribution to be the mass completeness limit at each redshift bin. For our K_S -band selected sample, the K_S -band limiting magnitude is the 5σ depth magnitude (22.4) measured in NEWFIRM. If we use this as m_{lim} in equation (2) to estimate the stellar mass completeness for sample S2-No-Lum-AGN, we find $\log(M_{*,95\% \text{lim}}/M_\odot) = 9.99, 10.42, 10.76, 11.12$ at $z = 0.5-1.0, z = 1.0-1.5, z = 1.5-2.0, z = 2.0-3.0$, respectively, for the mass completeness limit.

Although different bandpasses, such as the IRAC 3.6 and 4.5 μm bandpasses, are better suited to tracing the stellar mass build-up of galaxies at $z \sim 2$, the Pozzetti et al. (2010) method for estimating stellar mass completeness takes into account the range in mass-to-light (M/L) ratios at different redshifts using a bandpass that is not close to rest-frame K . We find that the stellar mass completeness limits do not change by more than ~ 0.1 dex at all redshifts if we use IRAC 3.6 μm -band photometry instead of K_S -band photometry to estimate stellar mass completeness. We also find similar stellar mass completeness limits when using 4.5 μm -band photometry to those estimated from K_S -band photometry (i.e. do not vary by more than ~ 0.1 dex) at $z < 2$. At $z = 2.0-3.0$, the stellar mass completeness

limits estimated from IRAC 4.5 μm -band photometry is 0.3 dex lower than when estimated from K_S -band photometry. Because our sample is a K_S -band selected sample, and stellar mass completeness limits do not vary much when using $K_S, 3.6$, or 4.5 μm -band photometry, we decide to use the K_S limiting magnitude and photometry to estimate stellar mass completeness.

Lastly, we apply this method to our sample of galaxies with X-ray luminous AGNs (S1-Lum-AGN) to estimate stellar mass completeness limits for that sample and find that the stellar mass completeness limits of S1-Lum-AGN are lower by 0.1–0.2 dex at $z < 1.5$, and by 0.3–0.5 dex at $z > 1.5$, when compared to those of our sample of galaxies without X-ray luminous AGNs (S2-No-Lum-AGN). We use the more stringent completeness limit found from S2-No-Lum-AGN as the stellar mass completeness limits for both samples in this analysis.

In Fig. 5, we plot the observed SMF of galaxies with (S1-Lum-AGN) and without (S2-No-Lum-AGN) X-ray luminous AGNs in four different bins of redshift across $z = 0.5-3$. The SMF is estimated using the $1/V_{\text{max}}$ method described in Section 2.4.1 for the X-ray luminosity function. The dashed line in each panel indicates the completeness limit of the sample S2-No-Lum-AGN. *The SMF for the sample (S1-Lum-AGN) of galaxies with X-ray luminous AGN shows that the number density of such systems is about three orders of magnitude lower than galaxies without X-ray luminous AGNs at $\log(M_*/M_\odot) < 11$ and about two orders of magnitude lower at $\log(M_*/M_\odot) > 11$, at all redshifts.* All galaxies in S1-Lum-AGN are complete in X-ray luminosity at each given redshift range, and AGN-host galaxies with $L_X > 10^{43} \text{ erg s}^{-1}$ have been shown to exhibit a turnover with decreasing number densities towards lower masses at $\log(M_*/M_\odot) < 11$ (Bongiorno et al. 2016), which is consistent with what we observe in our SMF of galaxies with X-ray luminous AGNs.

We compare the observed SMF of our sample of galaxies without X-ray luminous AGNs (S2-No-Lum-AGN) to the observed SMF from other studies in Fig. 6. We plot the observed values of Muzzin et al. (2013) and Ilbert et al. (2013) at $z = 0.5-2.5$ and the observed values of Kawinwanichakij et al. (2020) at $z \sim 0.75$ and $z \sim 1.25$. Our observed SMF for S2-No-Lum-AGN agrees well with those from other studies at all redshifts for galaxies with $\log(M_*/M_\odot) > 11$ and at all redshifts, except $z = 1.5-2.0$, at stellar masses above the 95 per cent completeness limit. The discrepancy between our SMF values and those of Muzzin et al. (2013) and Ilbert et al. (2013) at $z = 1.5-2.0$ could arise from a number of factors, such as cosmic variance, since both Muzzin et al. (2013) and Ilbert et al. (2013) probe the same small area ($<1.6 \text{ deg}^2$) on the sky, and/or a lack of photometric filters in our data that allow us to probe certain features in model spectra during SED fitting that can break degeneracies between different redshifts and cause us to miss certain galaxies at $z = 1.5-2.0$. Although we do not believe the latter to be the full cause of this discrepancy, we do not have other SMFs to compare to at this redshift range and our SMF agrees with that of Sherman et al. (submitted) at $z = 1.5-2.0$.

4.2 Distribution of star formation rates

In Fig. 7, we show the normalized SFR distribution for galaxies with (S1-Lum-AGN) and without (S2-No-Lum-AGN) X-ray luminous AGNs. The SFR histograms are normalized by dividing the number of galaxies in each bin by the total number of objects in the redshift bin, such that the sum of all the histogram bins is equal to 1. We remind the reader that the SFRs reported here are the instantaneous SFRs given by equation (1) in Section 3 from the SFH of the SED fit.

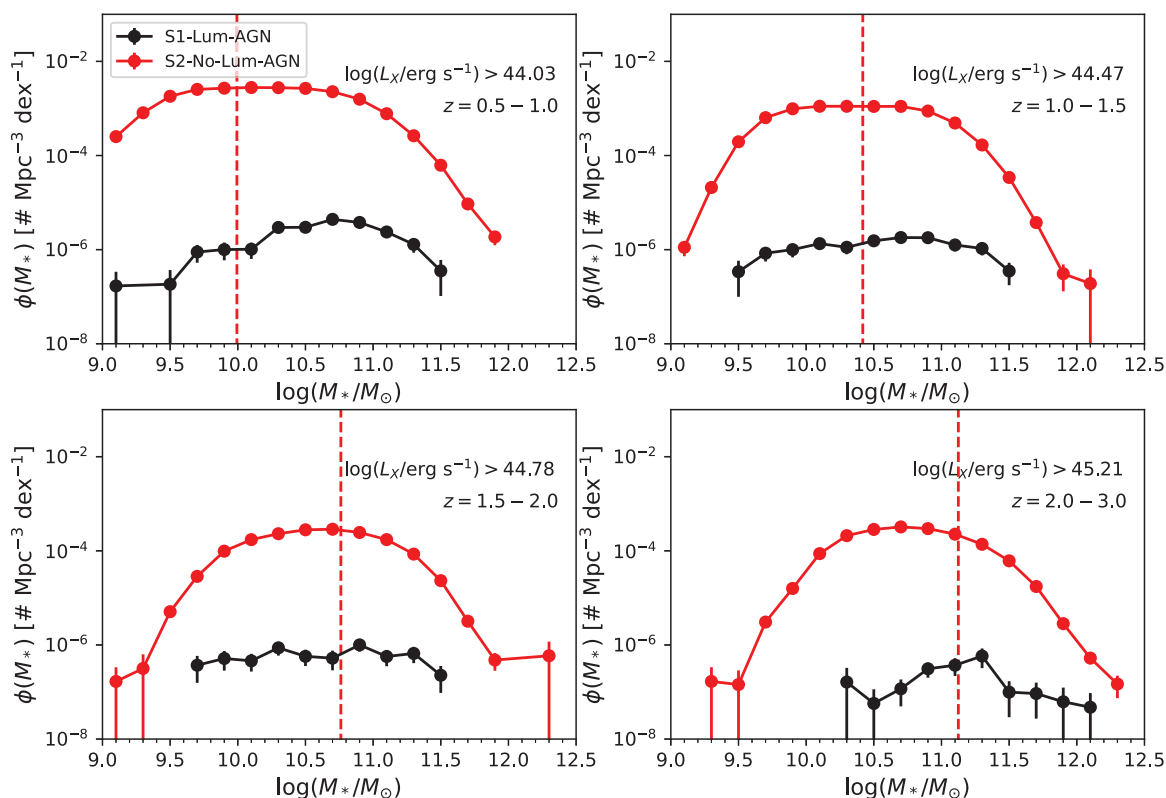


Figure 5. Galaxy stellar mass function (SMF) for our samples of galaxies with (S1-Lum-AGN, black) and without (S2-No-Lum-AGN, red) X-ray luminous AGNs at four different redshift ranges. All galaxies with X-ray luminous AGNs (S1-Lum-AGN) are complete in X-ray luminosity at their respective redshift bin; we show the X-ray completeness limit in each panel. The dashed vertical line indicates the stellar mass completeness of the sample of galaxies without X-ray luminous AGNs (S2-No-Lum-AGN) at each bin. The error bars at each stellar mass bin are Poisson errors. The SMF is calculated using the $1/V_{\max}$ correction described in Section 2.4.1 for the X-ray luminosity function. We find that the SMF of galaxies with X-ray luminous AGNs is much lower than the SMF of galaxies without X-ray luminous AGNs by ~ 2 orders of magnitude at $M_* > 10^{11} M_{\odot}$ and by ~ 3 orders of magnitude at $M_* < 10^{11} M_{\odot}$.

The SFR from an SED fit refers to the intrinsic extinction-corrected SFR and is typically constrained by fitting observed photometry ranging from the UV to the IRAC 4.5 μm band.

Fig. 7 shows that the SFRs for galaxies with X-ray luminous AGNs (S1-Lum-AGN) have a distribution skewed towards higher values, and therefore, have higher SFRs than galaxies without X-ray luminous AGNs (S2-No-Lum-AGN). The median SFR values for both samples at each redshift range is $\log(\text{SFR}/M_{\odot}\text{yr}^{-1}) = 1.18, 1.41, 1.77, 2.68$ for S1-Lum-AGN at $z = 0.5-1, z = 1-1.5, z = 1.5-2$, and $z = 2-3$, respectively, and $\log(\text{SFR}/M_{\odot}\text{yr}^{-1}) = 0.41, 0.96, 1.15, 1.49$ for S2-No-Lum-AGN, respectively. The median SFR values are roughly a factor of 5–10 higher for galaxies with X-ray luminous AGNs than galaxies without X-ray luminous AGNs.

It is often useful in studies of galaxy evolution to estimate the completeness limit down to which one can measure the SFR. This is not so easy to do for our analysis as our measured SFRs refer to the intrinsic extinction-corrected SFR derived by fitting observed photometry over a wide range of wavelengths from the UV to the IRAC 4.5 μm band using a large set of SED templates with many free parameters. Getting a true completeness limit for this measured SFR would be complicated and requires the analysis of many observed bands and SED templates. Instead, we attempt here to make a simpler estimate of the observed dust-extinguished FUV-based SFR by using the detection limits in just a few bands (DECam u and g bands) that trace the rest-frame UV luminosity from massive SF across our redshift range of interest.

For this estimate of the detection limit for the observed dust-extinguished SFR, we start by converting the observed magnitude closest to the rest-frame FUV wavelength into a luminosity (i.e. DECam u band at $z < 1.5$, DECam g band at $z > 1.5$). We then compute the 100 Myr FUV-based dust-extinguished SFR for our sample of galaxies without X-ray luminous AGNs (S2-No-Lum-AGN), using the SFR calibrator from Hao et al. (2011) and assume a Kroupa IMF (Kroupa 2001). The fact that SFRs computed in CIGALE assume a Chabrier (2003) IMF is not a problem as the shifts in SFR calculated from either IMF are essentially negligible (Speagle et al. 2014).

We estimate the 5σ completeness limit for the observed dust-extinguished FUV-based SFR similarly to how we estimate stellar mass completeness. That is, we take the 20 per cent faintest galaxies in each redshift bin, using the u -band at $z < 1.5$ and the g band at $z > 1.5$, and scale their FUV SFRs to the value they would have if their magnitude was equal to the limiting magnitudes of the survey (25.0 AB magnitude for u band, 24.8 AB magnitude for g band), which are the 5σ magnitude depths reported in Wold et al. (2019) using the following equation:

$$\log(\text{SFR}_{\text{FUV,lim}}) = \log(\text{SFR}_{\text{FUV}}) + 0.4(m - m_{\text{lim}}) \quad (3)$$

From the resulting distribution of values, we take the 95th percentile value as a lower limit to the 5σ completeness limit for the observed dust-extinguished FUV-based SFR. The values are $\log(\text{SFR}/M_{\odot}\text{yr}^{-1}) = -0.22, 0.23, 0.54$, and 0.92 at $z = 0.5-1.0, z = 1.0-1.5, z = 1.5-2.0$, and $z = 2.0-3.0$, respectively. We thus expect our survey to detect dust-extinguished FUV-based SFR above these values at the

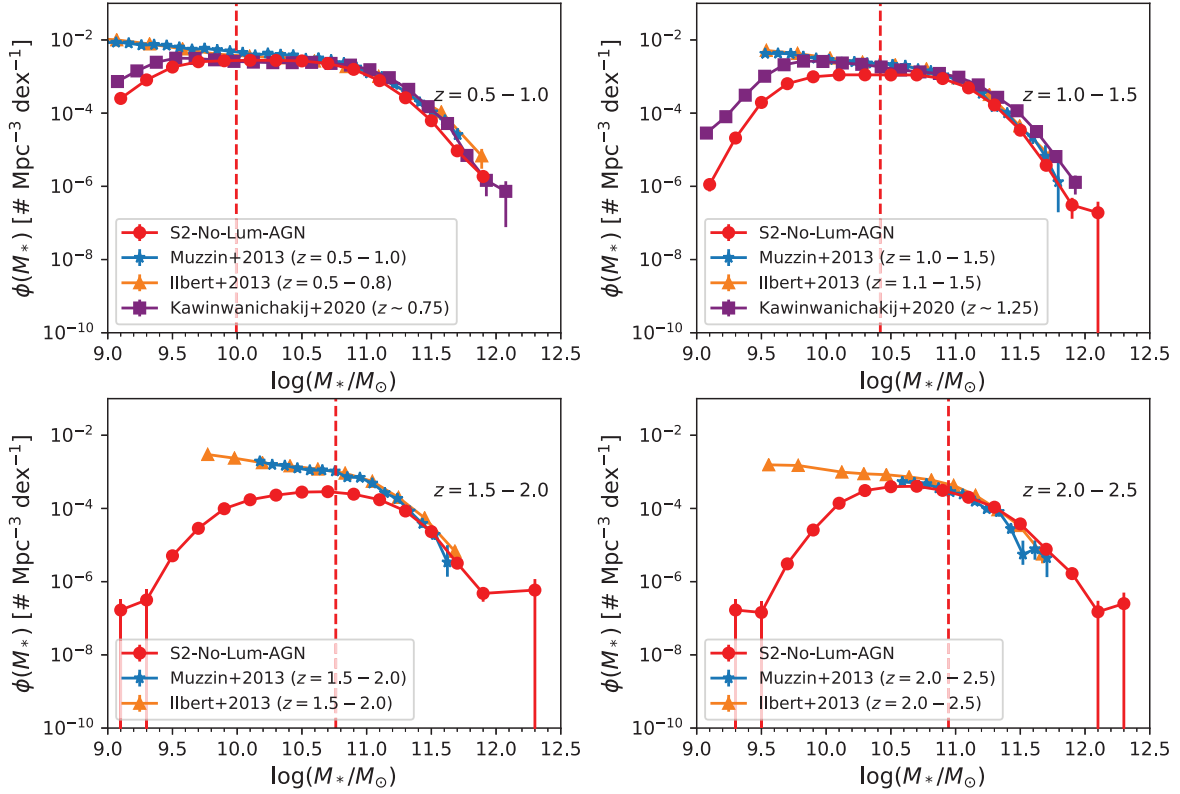


Figure 6. The observed galaxy SMF of our sample of galaxies without X-ray luminous AGNs (S2-No-Lum-AGN, red) in four redshift bins with observed literature values at the corresponding redshifts plotted from Muzzin et al. (2013) at $z = 0.5–2.5$ (blue, stars), Ilbert et al. (2013) at $z = 0.5–2.5$ (orange, triangles), and Kawinwanichakij et al. (2020) at $z \sim 0.75$ and $z \sim 1.25$ (purple, squares). As in Fig. 5 for our sample, the red dashed line represents the stellar completeness limit of our sample, error bars represent Poisson errors, and the SMF is calculated using the $1/V_{\max}$ method. We end the last redshift bin here at $z = 2.5$, instead of $z = 3.0$, for comparison purposes. We find good agreement with other observed SMFs at all redshifts for galaxies with $\log(M_*/M_\odot) > 11$ and at all stellar masses above our completeness limit for all redshift ranges except $z = 1.5–2.0$ (see text).

5σ level. In practice, we do not use an S/N cut for the u - or g -band fluxes in our analysis, so we should be able to measure dust-extinguished FUV-based SFRs below these 5σ limit values.

We plot our estimated 5σ completeness limit for the observed dust-extinguished FUV-based SFR as dotted lines in Fig. 7, which also shows the distribution of measured SFRs for the samples of galaxies with (S1-Lum-AGN) and without (S2-No-Lum-AGN) X-ray luminous AGNs. It is important to bear in mind that the measured SFRs from the SED fit and the observed dust-extinguished FUV-based SFRs are two very different quantities. The measured SFRs from the SED fit refer to the intrinsic dust-corrected SFR of a galaxy based on the SED fit and observed photometry from the UV to the IRAC $4.5 \mu\text{m}$ band and are likely higher than the observed dust-extinguished FUV-based SFRs. The fact that we see some measured intrinsic SFR values lower than the 5σ completeness limit for the observed dust-extinguished FUV-based SFR is likely due to the fact that we do not use an S/N cut for the u - or g -band fluxes in our analysis.

4.3 Testing CIGALE SFRs against previously published empirical SFRs

In this section and the following section, we explore whether the SFRs derived by CIGALE for galaxies hosting X-ray luminous AGNs are reliable by performing two separate tests that are based, respectively, on previously published SFRs of real galaxies with X-ray luminous AGNs and a set of synthetic mock galaxy SEDs.

For the first test, we compare SFRs derived from CIGALE with SFRs from the CANDELS catalogue (Grogin et al. 2011; Koekemoer et al. 2011), where SFRs are derived from SED fitting using near-UV to near-IR photometry (see Yang et al. 2019, 2017, for description of SFR estimates). The SFRs presented in Yang et al. (2019) are median values of SFRs obtained from separate teams who perform SED fitting of the same sample and take the total SFR values from the SFH of the SED fit. We do not use the FIR-derived SFRs presented in Yang et al. (2019), Yang et al. (2017) as they are not corrected for AGN emission and thus would overestimate the SFR when converting between FIR luminosity and SFR (see Section 3.1 and Fig. 3). We select 38 sources in the CANDELS catalogue with a *Chandra* X-ray detection with $L_X > 10^{43} \text{ erg s}^{-1}$ in order to obtain SFRs, using CIGALE, for a sample of galaxies with X-ray luminous AGNs. For these sources, we select available photometry from the COSMOS and Ultra-deep Survey (UDS) fields in CANDELS [i.e. CFHT MegaCam u , g , r , i , z bands, NEWFIRM K_S band (van Dokkum et al. 2009), IRAC 3.6 and $4.5 \mu\text{m}$] to perform SED fitting using photometric bands that cover the same wavelength ranges that we use to perform SED fitting of our S1-Lum-AGN and S2-No-Lum-AGN samples. We also adopt the redshifts from the CANDELS catalogue when we perform the SED fit in CIGALE.

In Fig. 8, we show the SFRs obtained for the CANDELS sample described above using CIGALE to the published SFR values of the CANDELS catalogue described in Grogin et al. (2011) and Koekemoer et al. (2011). Only at the highest SFRs does the mean CANDELS SFR deviate from the one-to-one line by a factor of

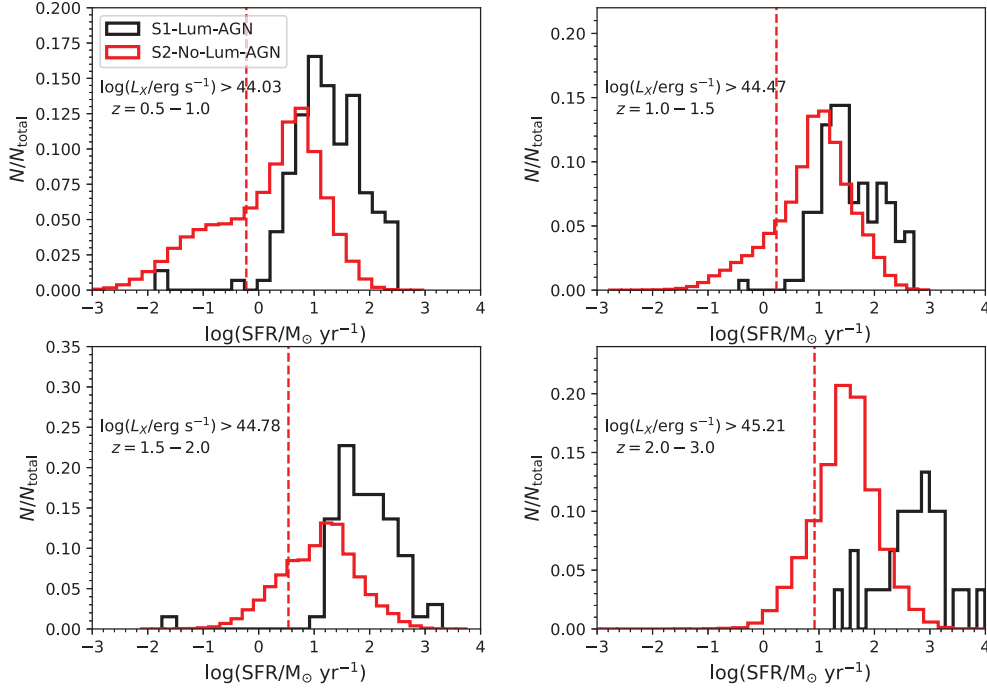


Figure 7. We plot the normalized histograms of the log of the measured SFR for our sample of galaxies with (S1-Lum-AGN, black) and without (S2-No-Lum-AGN, red) X-ray luminous AGNs across four different redshift bins. The measured SFR refers to the intrinsic dust-corrected SFR derived from the SFH produced by SED fitting with CIGALE of the observed photometry from the UV to the IRAC 4.5 μm band. Note that galaxies with X-ray luminous AGNs have a distribution of intrinsic SFRs skewed towards higher values than galaxies without X-ray luminous AGNs. We also plot as dotted lines our estimated 5σ completeness limit for the observed dust-extinguished FUV-based SFR, which is estimated from the 5σ detection limit in the u -band and g -band filters, which most closely trace the rest-frame 1500 \AA luminosity at $z = 0.5-1.5$ and $z = 1.5-3.0$, respectively. See text in Section 4.2 for details.

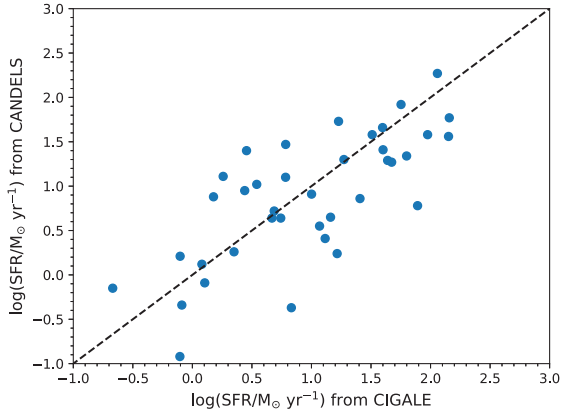


Figure 8. SFRs from CANDELS (y-axis) compared to SFRs derived from CIGALE using CFHT (u, g, r, i, z), NEWFIRM (K band), and IRAC (3.6 and 4.5 μm) photometry for a sample of 38 galaxies with X-ray luminous AGNs having $L_X > 10^{43} \text{ erg s}^{-1}$. Also shown is the one-to-one line (dashed, black).

~ 0.5 dex and we note only one source has an SFR that varies by an order of magnitude between the CIGALE SFR and CANDELS reported SFRs.

4.4 Testing CIGALE SFRs against SFRs from mock SEDs

In this section, we explore whether the SFRs derived by CIGALE for galaxies hosting X-ray luminous AGNs are reliable by performing tests on a set of synthetic mock galaxy SEDs. We use CIGALE to generate mock galaxy SEDs with AGN emission and then perform SED fitting on the mock galaxy SED fluxes. We generate two sets of

mock galaxy SEDs using the stellar population synthesis models of Bruzual & Charlot (2003), assume a Chabrier (2003) IMF, and for one set of mocks we employ the Fritz et al. (2006) AGN emission templates with an updated version of the Draine & Li (2007) dust emission models, and for the other set of mocks we employ the Dale et al. (2014) combined dust and AGN emission models. We use varying dust and AGN emission templates when generating mock galaxy SEDs in order to test whether CIGALE can recover the properties of mock galaxies produced with varying models using the same emission templates discussed in Section 3.

When we generate mock galaxy SEDs in CIGALE, we obtain mock observation fluxes in the DECam u, g, r, i, z bands, NEWFIRM K band, and IRAC 3.6 and 4.5 μm bands. In order to assign flux errors for a given photometric band, we calculate the mean S/N of all sources in our data as a function of magnitude. We then use this mean S/N to assign flux errors to mock sources depending on what their magnitude is. This method produces reasonable flux errors in the mock photometry that match our data. At this stage we perturb the fluxes within the errors by drawing from a normal distribution centred around the mock flux with a standard deviation equal to the photometric error. With the new photometric fluxes and flux errors, we perform the same cuts on the mock objects as the real data to obtain a mock photometric sample that resembles our data in terms of magnitude and S/N ratios. That is, we only perform SED fitting on sources with an S/N greater than 5 in the K_S band, an S/N greater than 2 in the two IRAC bands, and require a flux detection in the u, g, r, i, z bands.

In Fig. 9, we compare the SFR derived from SED fitting with CIGALE to the true SFR of the mock galaxy. We only show the results for the mock galaxies generated from the Fritz et al. (2006) and Draine & Li (2007) AGNs and dust emission templates. However,

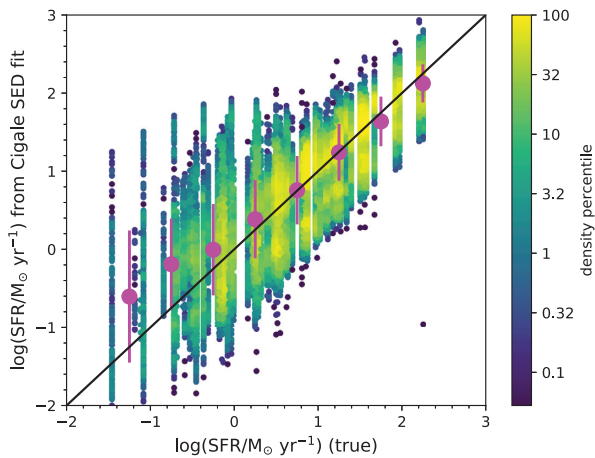


Figure 9. Comparison of SFRs from the mock galaxies (x-axis) versus SFRs obtained from the SED fit with CIGALE to the mock galaxy fluxes (y-axis). We do not include WISE photometry in this test in order to resemble the fits we are doing with our S1-Lum-AGN sample. Also shown is the one-to-one line and the mean of the $\log(\text{SFR})$ (magenta circles) with the standard deviation represented by the error bars. All points are colour-coded by their density on the x (mock SFR) and y (fit SFR) plane, where density is calculated by counting number of neighbours around each data point inside a circular aperture. We find relatively good agreement between the true SFRs of the mock galaxies and the CIGALE-derived SFRs above $\sim 1 M_{\odot} \text{yr}^{-1}$. At the low end of the true SFRs, some mock galaxies have high CIGALE-derived SFRs, however, only 2 per cent of the mock galaxies have true SFRs that differ from their CIGALE-derived SFR by a factor of 10 or more and only 10 per cent of mock galaxies have true SFRs that differ from the CIGALE-derived SFRs by a factor of 4 or more.

our results do not change for the mock galaxies where AGNs and dust emission is generated from the Dale et al. (2014) templates, suggesting that the choice of AGNs or dust emission templates in CIGALE should not have a large impact on the results.

In Fig. 9, we see good agreement between the CIGALE-derived SFRs and the true SFRs of mock galaxies above $\sim 1 M_{\odot} \text{yr}^{-1}$ with a scatter of 0.5 dex. At the low SFR end there are some mock galaxies for which the CIGALE-derived SFRs are significantly higher than the true SFRs. However, only 2 per cent of the mock galaxies have $|\Delta \log(\text{SFR})| > 1$ [where $\Delta \log(\text{SFR}) = \log(\text{SFR}_{\text{fit}}) - \log(\text{SFR}_{\text{true}})$] and only 10 per cent of mock objects have $|\Delta \log(\text{SFR})| > 0.6$, meaning 90 per cent of our mock sample has true SFRs that agree with the CIGALE-derived SFRs to within a factor of 3–4. Most of the large scatter between the true and fit SFRs lie at low SFRs ($< 1 M_{\odot} \text{yr}^{-1}$), however, we note that most (> 80 per cent) of our sample have SFRs above $1 M_{\odot} \text{yr}^{-1}$. At the low end of the true SFRs, some mock galaxies have high CIGALE-derived SFRs, however, only 2 per cent of the mock galaxies have true SFRs that differ from their CIGALE-derived SFR by a factor of 10 or more and only 10 per cent of mock galaxies have true SFRs that differ from the CIGALE-derived SFRs by a factor of 4 or more. We find that CIGALE does not produce a systematic bias towards higher or lower values of SFRs when recovering SFRs from the true mock galaxy SEDs.

5 RESULTS

In the following section, we compare the properties of the sample galaxies with (S1-Lum-AGN) and without (S2-No-Lum-AGN) X-ray luminous AGNs at fixed redshift and stellar mass. Many studies

have looked at the evolution of SFR with stellar mass across redshift (Daddi et al. 2007; Elbaz et al. 2007; Speagle et al. 2014; Whitaker et al. 2014), however, galaxies with X-ray luminous AGNs are usually not included in these studies due to AGN emission contaminating the UV and IR wavelengths. Although there have been a few studies that look at the relation between stellar mass and SFR of galaxies with luminous AGNs (Santini et al. 2012; Shimizu et al. 2015; Masoura et al. 2018), they do not derive stellar masses and SFRs for their galaxy samples with and without luminous AGNs in a self-consistent manner, and their control sample of galaxies without luminous AGNs is at least an order of magnitude smaller than the control sample (S2-No-Lum-AGN) in our study.

5.1 SFR as a function of stellar mass and redshift

In Fig. 10, we show the stellar mass and SFR of our sample of galaxies with (S1-Lum-AGN) and without (S2-No-Lum-AGN) X-ray luminous AGNs. The galaxies in S2-No-Lum-AGN are colour-coded by their density on the stellar mass-SFR plane, where density is calculated by counting number of neighbours around each data point inside a circular aperture with a radius equal to 0.05. The colour bar shows the percentile value of the data point's density, where the 100th percentile value corresponds to the highest density and the 0.1 percentile value corresponds to the data points whose density is 1/10th the maximum density. Also shown in Fig. 10 is the mean SFR in different bins of stellar mass for S2-No-Lum-AGN, which we refer to as the main sequence, with 1σ errors calculated through a bootstrap method. We calculate errors in the mean SFR by resampling (i.e. drawing randomly from) the SFR distribution inside a bin of stellar mass x times, where x is the number of objects inside the bin, build a sample from the random draws and calculate the mean for that sample. We draw objects with replacement so the same object in a given bin can be sampled more than once. We do this 1000 times and make a distribution of mean SFR values from each resampling and take the 16th and 84th percentile of this distribution to calculate the error on the mean of the SFR.

We make note of the four galaxies with X-ray luminous AGNs (S1-Lum-AGN) in Fig. 10 that have SFRs low enough to be considered outliers with respect to the rest of the galaxies in S1-Lum-AGN on the mass-SFR plane. Two of these objects exist at $z = 0.5-1.0$, one object exists at $z = 1.0-1.5$, and one object exists at $z = 1.5-2.0$. We have inspected the DECam and IRAC images, the flags in the source extractor catalogues, as well as the quality of the SED fits of the two outliers at $z = 0.5-1$ and the two outliers at $z = 1-1.5$ and $z = 1.5-2$. The inspection revealed nothing out of the ordinary or anything that could impair the photometry for these objects. Furthermore, the reduced χ^2 of the SED fit to the photometry is less than 5 in all cases, indicating a good fit. As a result, we have no reason to believe that the measured SFRs are erroneous.

In Fig. 11, we show the mean SFRs of our sample of galaxies with (S1-Lum-AGN) and without (S2-No-Lum-AGN) X-ray luminous AGNs as a function of stellar mass across four redshift bins. Error bars are determined from the bootstrap method described above. In all redshift bins, we find that the mean SFRs of galaxies with X-ray luminous AGNs are higher by a factor of 3–10 than those of galaxies without X-ray luminous AGNs at a given stellar mass. This suggests that X-ray luminous AGNs tend to coexist in galaxies with enhanced SFRs. In Section 6, we discuss how these results fit into possible evolutionary scenarios connecting AGN and SF activity.

Our results are consistent with those of Santini et al. (2012) who find that the SF activity of galaxies with luminous AGNs is enhanced with respect to a mass-matched sample of inactive galaxies

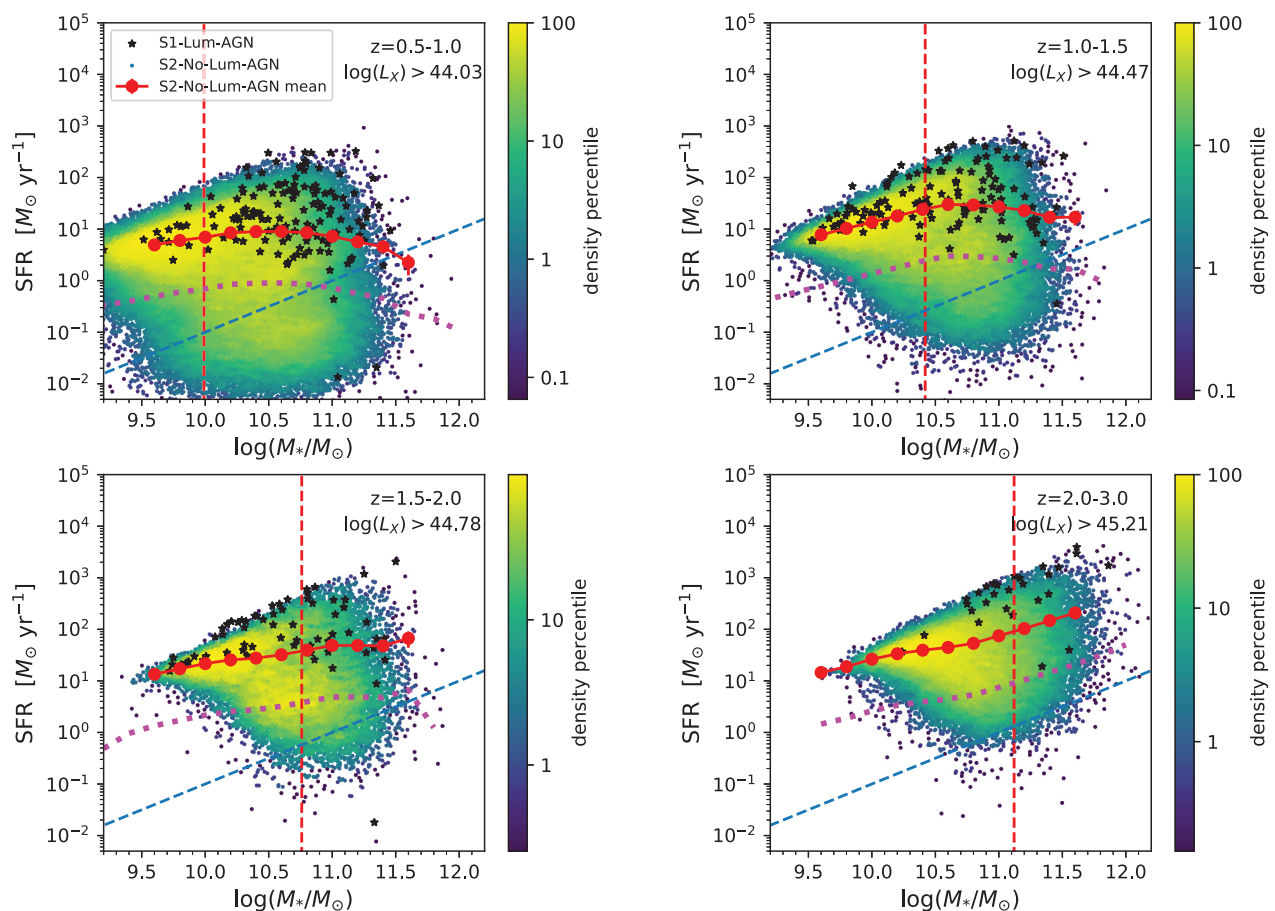


Figure 10. SFR versus stellar mass for our sample of galaxies with (S1-Lum-AGN, black stars) and without (S2-No-Lum-AGN, coloured points) X-ray luminous AGNs in four different redshift bins. The S2-No-Lum-AGN galaxies are colour-coded by their density on the stellar mass–SFR plane (see text). The dashed vertical line on each panel shows the stellar mass completeness limit in that bin (see Section 4.1). The X-ray completeness limit for S1-Lum-AGN is shown in each redshift bin in log units of ergs per second. Also shown are the mean SFR of S2-No-Lum-AGN as a function of stellar mass (red circles), which we refer to as the main sequence, the line that falls 1 dex below the main sequence (dotted magenta) and the line where the specific SFR is 10^{-11} yr^{-1} (blue dashed). It is striking that galaxies with X-ray luminous AGNs have higher mean SFRs than galaxies without X-ray luminous AGNs at a given stellar mass (see also Fig. 11). Note also that very few galaxies with X-ray luminous AGNs have quenched SF if we use the common definition of quenched galaxies as having a specific SFR $< 10^{-11} \text{ yr}^{-1}$.

(i.e. galaxies without AGN activity) at $z = 0.5–2.5$. Furthermore, they find that the level of enhancement in SF activity amongst galaxies with luminous AGNs is higher for galaxies with high X-ray luminosities ($L_X > 10^{43.5} \text{ ergs}^{-1}$). Our results are also consistent with those of Masoura et al. (2018) who compare the mean SFRs of their sample of galaxies with X-ray luminous AGNs to the SFR values of star forming galaxies from Schreiber et al. (2015) at fixed stellar mass and find that the mean SFRs at fixed mass of galaxies with X-ray luminous AGNs are higher than those of galaxies without X-ray luminous AGNs. We also find that our results are consistent with those of Kirkpatrick et al. (2019b) and Kirkpatrick et al. (2019a). In Kirkpatrick et al. (2019b), they find that AGNs from $z = 1–4$ have high SFRs and star formation efficiencies and show no signs of quenching. Kirkpatrick et al. (2019a) find that some of the most luminous quasars in Stripe 82 at $z = 1–2$ have the highest SFRs that are a factor of $\sim 3–7$ above the main sequence.

The results in Shimizu et al. (2015) may appear to contradict the results we find here, as they claim their sample of AGN-host galaxies appear to have SFRs that fall off the main sequence of star forming galaxies. However, a subsequent paper Shimizu et al. (2017) claims that when they mass-match their sample of AGN-host

galaxies to a control sample, the AGN-host galaxies have higher SFR on average. The erroneous result in Shimizu et al. (2015) is explained by a mismatch between their sample of AGN-host galaxies and their comparative control sample: the mass distribution of their AGN-host galaxies is shifted towards higher values than the mass distribution of their sample of star forming galaxies, and thus, their AGN-host galaxies have lower specific SFR values typical of higher mass ($M_* > 10^{10.5} M_\odot$) galaxies.

In summary, we find that the mean SFR in galaxies with X-ray luminous AGNs is significantly larger than in galaxies without X-ray luminous AGNs at a given stellar mass. Our results are consistent with those from several earlier studies described above, but they are significantly more robust because our sample of galaxies without X-ray luminous AGNs is 10–100 times larger than those of earlier studies, and we analyse both our AGN sample (S1-Lum-AGN) and our mass-matched non-AGN sample (S2-No-Lum-AGN) using the same SED fitting code and methodology. Our results are consistent with a scenario where the high SFR and AGN luminosity are triggered by processes that produce large gas inflow rates into the regions (on scales of a few hundreds to few kpc) typically associated with high SFRs, as well as the sub-pc region associated with the AGN

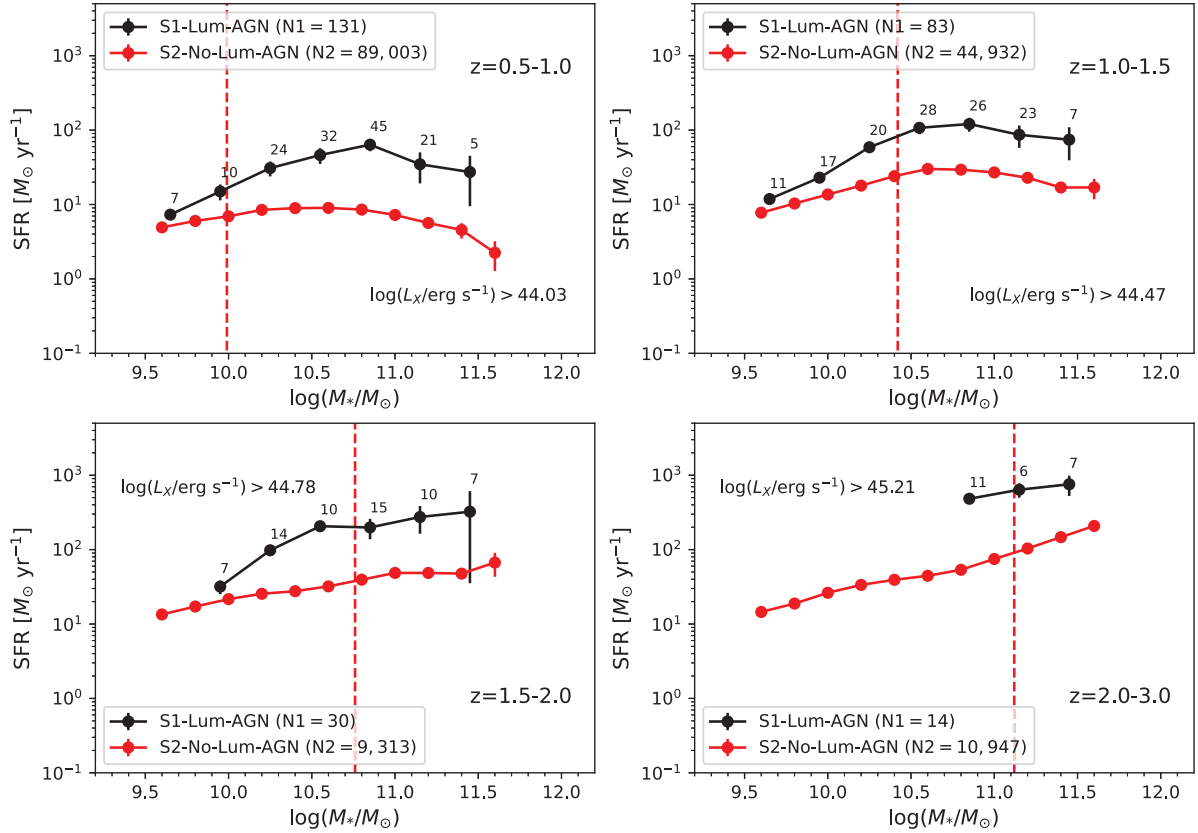


Figure 11. The mean SFRs for our sample of galaxies with (S1-Lum-AGN, black circles) and without (S2-No-Lum-AGN, red circles, same as those shown in Fig. 10) X-ray luminous AGNs as a function of stellar mass across four redshift bins. We show the total number (N1 and N2) of galaxies in each sample above the stellar mass completeness limit (shown here as vertical dashed lines), as well as the number of galaxies with X-ray luminous AGNs in each stellar mass bin above the X-ray luminosity completeness limit. Error bars are 1σ values from a bootstrap analysis. The mean SFRs of galaxies with X-ray luminous AGNs are higher by a factor of 3–10 than those of galaxies without X-ray luminous AGNs at a given stellar mass.

accretion disc. We refer the reader to Section 6 for a more detailed discussion of potential evolutionary sequences between AGN and SF activity.

5.2 Properties and fraction of galaxies with quenched star formation

In this section, we explore the quenched fraction of our sample of galaxies with (S1-Lum-AGN) and without (S2-No-Lum-AGN) X-ray luminous AGNs at fixed stellar mass. The processes that quench SF (i.e. significantly suppress SF) are important for our understanding of galaxy evolution as they intimately regulate the growth of the stellar mass in galaxies. Theorists often invoke AGN feedback in simulations as a way to quench SF (Hambrick et al. 2011; Fabian 2012; Vogelsberger et al. 2013; Choi et al. 2015; Roos et al. 2015; Hopkins et al. 2016; Bieri et al. 2017) in massive galaxies and prevent the overproduction of massive galaxies relative to the observed mass and luminosity functions. By measuring the quenched fraction of massive galaxies with and without X-ray luminous AGNs, we aim to shed light on the role of quenching mechanisms, such as AGN feedback. While most earlier studies estimate the mean quenched fraction (averaged over massive galaxies) in different redshift ranges, the unprecedented size of our sample of massive galaxies (e.g. $\sim 30\,000$ galaxies with $M_* > 10^{11} M_\odot$) enables us to study how the quenched fraction (f_{quenched}) varies with stellar mass at different redshifts (Fig. 12).

In the literature, multiple methods are used to identify quenched galaxies. Numerous works define quenched galaxies as galaxies having specific SFR (sSFR) less than 10^{-11} yr^{-1} (Fontanot et al. 2009; Stefanon et al. 2013). Given the bimodality in colour and star formation, it is also common to separate quenched galaxies from star-forming galaxies using a selection based on $U - V$ and $V - J$ colours (UVJ diagram, Wuyts et al. 2007; Whitaker et al. 2011; Muzzin et al. 2013; Fang et al. 2018). In Fang et al. (2018) and Donnari et al. (2019), a separate method used to define quiescence based on distance from the main sequence is introduced, where galaxies that fall 1 dex or 2σ below the main sequence are defined as quenched.

For this work, we select quenched galaxies based on a galaxy's sSFR ($\text{sSFR} < 10^{-11} \text{ yr}^{-1}$) and based on distance from the main sequence of star formation. In Fig. 10, the blue dashed line represents sSFR of 10^{-11} yr^{-1} . If we follow the approach of Fontanot et al. (2009), where quenched galaxies are defined as having a sSFR $< 10^{-11} \text{ yr}^{-1}$, then Fig. 10 shows that very few galaxies with X-ray luminous AGNs (< 5 per cent) have quenched SF. For the second definition of quiescence based on distance from the main sequence, we define a quiescent sample using an approach similar to Donnari et al. (2019) and select our quenched sample in four different redshift ranges spanning $0.5 < z < 3$. The quenched galaxies we select using this method are galaxies whose SFR is at least 1 dex below the main sequence. We rely on this second method of defining quiescence because it allows one to measure the quenched fraction of galaxies in observations without having to worry about the discrepancies that

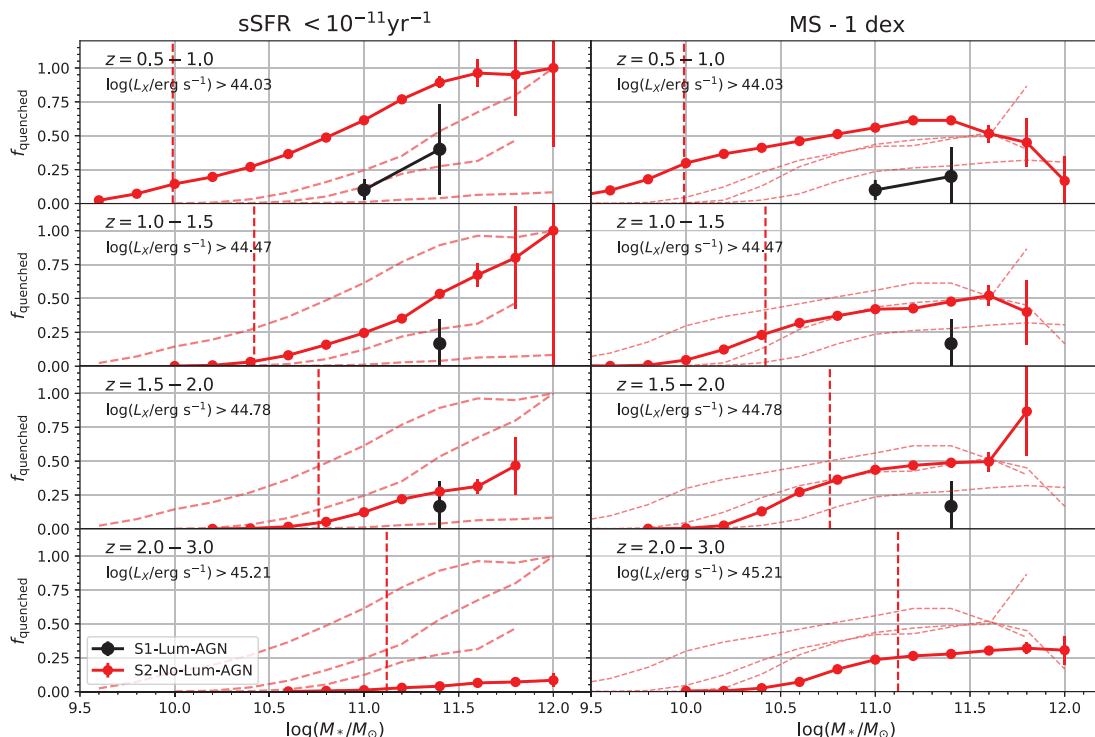


Figure 12. This figure shows the quenched fraction as a function of stellar mass in four different bins of redshift spanning $z = 0.5–3$ using two definitions of quiescence, whereby quenched galaxies are defined as having a $sSFR < 10^{-11} \text{ yr}^{-1}$ (left-hand panels) or as having an SFR at least 1 dex below the main sequence at a given stellar mass (right-hand panels). In all panels, we plot the fraction of galaxies that are quenched among the sample of galaxies with (S1-Lum-AGN; black circles) and without (S2-No-Lum-AGN; red circles) X-ray luminous AGNs. The small dashed red lines in each panel represent the quenched fraction of S2-No-Lum-AGN in all the redshift ranges for easy visualization of the evolution of the quenched fraction with redshift. Poisson errors are shown on this plot as error bars. The quenched fractions based on the two definitions of quiescence are roughly consistent at $z < 1.5$, but differ significantly at higher redshifts ($z = 1.5–3$) where the quenched fraction based on $sSFR$ is lower by a factor of $\sim 2–3$ at $z = 1.5–2$ and by a factor of $\sim 5–10$ at $z = 2–3$ for galaxies with $M_* > 10^{11} M_\odot$. The quenched fractions are a strong function of stellar mass in each redshift bin and generally increase with stellar mass, except possibly at the very highest stellar masses.

arise in the measured stellar mass and SFR values amongst different SED fitting codes, which could affect the measured quenched fraction if selecting galaxies based on $sSFR$. In Fig. 10 the red line represents the main sequence, which is the mean SFR at fixed stellar mass for galaxies without X-ray luminous AGNs, and the dotted magenta line represents the region of the mass–SFR plane that falls exactly 1 dex below the main sequence, meaning any sources that exist below this line satisfy the aforementioned definition of quiescence. We do not use the UVJ diagram method to select quenched galaxies as galaxies with X-ray luminous AGNs, typically type I AGN-hosts or quasars, may have extremely blue colours due to emission from the accretion disc and thus affect our selection of quenched objects amongst the sample of galaxies with X-ray luminous AGNs. For galaxies with X-ray luminous AGNs with L_X above the 80 per cent completeness limit ($L_X = 10^{44.03}, 10^{44.47}, 10^{44.78}$, and $10^{45.21} \text{ erg s}^{-1}$, respectively, at $z = 0.5–1.0$, $z = 1.0–1.5$, $z = 1.5–2.0$, and $z = 2.0–3.0$), the vast majority (97 per cent, 98 per cent, 96 per cent, and 100 per cent, respectively, at $z = 0.5–1$, $z = 1.0–1.5$, $z = 1.5–2.0$, and $z = 2.0–3.0$) do not show quenched SF.

In Fig. 12, we show how the quenched fraction (f_{quenched}) varies with stellar mass in four different redshift bins for the two definitions of quiescence that we use here. Fig. 12 has two solid curves that represent the fraction of galaxies that are quenched among our two samples: the sample of galaxies with (S1-Lum-AGN) and without (S2-No-Lum-AGN) X-ray luminous AGNs. The three dashed lines in

each panel of Fig. 12 correspond to the quenched fraction of the S2-No-Lum-AGN sample in all redshift ranges for easy visualization of the evolution of the quenched fraction with redshift. The error bars represent Poisson errors. The sample without (S2-No-Lum-AGN) X-ray luminous AGNs is a factor of ~ 100 to ~ 1000 larger than the sample of galaxies with (S1-Lum-AGN) X-ray luminous AGNs, so we expect its behaviour to be representative of the underlying sample of all galaxies.

We find that the quenched fractions for galaxies without X-ray luminous AGNs, based on the two definitions of quenched galaxies ($sSFR < 10^{-11} \text{ yr}^{-1}$ versus SFR at least 1 dex below the main sequence) differ at all redshifts, especially at the highest redshift bin ($z = 2–3$) where the quenched fraction based on $sSFR$ is lower by a factor of $\sim 5–10$ at $z = 2–3$ for galaxies with $M_* > 10^{11} M_\odot$. These results are not surprising, as one definition of quiescence ($sSFR < 10^{-11} \text{ yr}^{-1}$) ignores the evolution with time of the SFR–stellar mass relation (Speagle et al. 2014; Whitaker et al. 2014), while the other definition of quiescence (SFR at least 1 dex below the main sequence) is based on a main sequence that is allowed to evolve as it is empirically determined in each redshift bin.

We also note that the value of the quenched fraction based on selecting quenched galaxies using their distance from the main sequence is more robust across different studies than the quenched fraction based on a specific value of the $sSFR$. This is because the latter is highly sensitive to systematic effects, such as those introduced

by the different fitting assumptions (e.g. different IMF, treatment of attenuation, choice of SPS, etc.) used by different SED fitting codes, impacting the absolute value of SFRs. For example, we find after running multiple tests that CIGALE produces systematically higher SFRs than EAZY-py by a factor of $\sim 2-3$, meaning that the measured quenched fractions (given by $sSFR < 10^{-11} \text{ yr}^{-1}$) would be higher for our sample if we use EAZY-py instead of CIGALE to derive SFRs. Fig. 12 shows that the quenched fractions based on both definitions of quiescence are a strong function of stellar mass in each redshift bin and generally increase with stellar mass, except possibly at the very highest stellar masses.

While many earlier studies with smaller samples measured the mean quenched fraction, averaged over stellar mass as a function of redshift (Kriek et al. 2006; Muzzin et al. 2013; Stefanon et al. 2013; Brennan et al. 2015; Fang et al. 2018), very few studies (e.g. Muzzin et al. 2013) measure the quenched fraction as a function of stellar mass over different redshift ranges. Our study is the first to reveal, using such a large sample of massive galaxies, how the quenched fraction (f_{quenched}) at a given redshift changes as the galaxy stellar mass varies from $10^{10} M_{\odot}$ to a few times $10^{11} M_{\odot}$ (Fig. 12). The fact that f_{quenched} rises with stellar mass provides important clues on the mechanisms that quench SF in massive galaxies.

6 DISCUSSION

In Section 5.1, we found that the average SFRs of galaxies with X-ray luminous AGNs are higher by a factor of $\sim 3-10$ compared to galaxies without X-ray luminous AGNs at a given stellar mass and redshift range (see Figs 10 and 11). These results are consistent with a scenario where the high SFR and high AGN luminosity are produced by processes that produce large gas inflow rates both into the regions (on scales of a few hundred pc to few kpc) typically associated with high SFRs, as well as the sub-pc region associated with the AGN accretion disc. Assuming a radiative efficiency of $\epsilon = 0.1$, and a bolometric to X-ray luminosity ratio of $L_{\text{bol}}/L_X \sim 30$ (Lusso et al. 2012), we estimate that the black hole accretion rates of our sample above the 80 per cent X-ray completeness limit exceed values of $0.48 M_{\odot} \text{ yr}^{-1}$ (for $L_X > 10^{44.03} \text{ erg s}^{-1}$ at $z = 0.5-1.0$), $1.3 M_{\odot} \text{ yr}^{-1}$ (for $L_X > 10^{44.47} \text{ erg s}^{-1}$ at $z = 1.0-1.5$), $2.7 M_{\odot} \text{ yr}^{-1}$ (for $L_X > 10^{44.78} \text{ erg s}^{-1}$ at $z = 1.5-2.0$), and $7.3 M_{\odot} \text{ yr}^{-1}$ (for $L_X > 10^{45.21} \text{ erg s}^{-1}$ at $z = 2.0-3.0$). Given our maximum X-ray luminosity in each redshift bin, we expect the black hole accretion rates to not exceed values of 14, 45, 50, and $100 M_{\odot} \text{ yr}^{-1}$ at $z = 0.5-1.0$, $z = 1.0-1.5$, $z = 1.5-2.0$, and $z = 2.0-3.0$, respectively.

Examples of processes that drive large gas inflow rates through gravitational torques, tidal torques, and dissipative shocks include gas-rich major mergers, gas-rich minor mergers, and strong tidal interactions in gas-rich systems. It should be noted that in order to drive gas from kpc scales down to the scales of the AGN accretion disc, we need mechanisms that effectively reduce the angular momentum of the gas by several orders of magnitude, such as gravitational torques from a primary bar, secondary bars or/and other non-axisymmetric features, shocks, dynamical friction on gas clumps, feedback processes from local SF, run-away self-gravitational instabilities, tidal disruption of clumps, and hydro-magnetic winds (e.g. Jogee 2006, and references therein). Another mechanism which can effectively reduce angular momentum has to do with the ram-pressure shocks described in Capelo & Dotti (2017), where large-scale (few kpc) shocks affect the entire galactic disc and decouple the dynamics of the gas from the stars and are a complementary trigger to tidal torques (see fig. 2 of Capelo & Dotti 2017).

It is instructive to look at numerical high-resolution simulations which explore the onset of high SFR and high AGN luminosity (Springel, Di Matteo & Hernquist 2005; Cox et al. 2008; Di Matteo et al. 2008; Capelo et al. 2015; Park, Smith & Yi 2017). In particular, the more recent numerical simulations of merging galaxies (e.g. Capelo et al. 2015; Park et al. 2017) show that large gas inflows during major mergers can simultaneously trigger SF and AGN activity in the merging galaxies. In these simulations, the peak of black hole accretion of SF activity appear to coincide and the decline of black hole accretion rate appears to trace the decline in SF with time. Park et al. (2017) and Capelo et al. (2015) show that AGN and SF activity are also triggered during minor mergers, but to a much lesser extent. In simulations of isolated galaxies, however, black hole accretion does not necessarily trace SF across time in the same way (Negri & Volonteri 2017). This can be due to the fact that in some isolated systems, SF can happen on very large scales (e.g. kpc to tens of kpc) without any associated AGN activity. In isolated barred galaxies, the primary stellar bar can efficiently drive gas down to scales of a few hundred pc to fuel circumnuclear SF activity (e.g. Elmegreen 1994; Knapen et al. 1995; Hunt & Malkan 1999; Jogee, Scoville & Kenney 2005), but in many cases the gas stalls on scales of a few hundred pc as there are no effective mechanisms to further rapidly drain its angular momentum and drive it down to the sub-pc scales of the AGN accretion disc (e.g. see Jogee 2006, and references therein).

Fig. 10 shows that galaxies that have moderate to low SFRs with respect to the average SFR (shown as the red curve) are not associated with X-ray luminous AGNs. There are several ways to explain these results. In the aforementioned Park et al. (2017) and Capelo et al. (2015) simulations of gas-rich major mergers, the contemporaneous phase of high SFR and AGN activity is followed by a phase where the black hole accretion rate and SFR both decline with time. In this scenario, the factors responsible for depressing SF (e.g. a declining gas supply, the heating or redistribution of the gas via stellar or AGN feedback) are also effective at depressing any AGN activity. We note that although the results in these simulations are for lower-mass galaxies than the ones we examine here, these simulation are of isolated systems and the results should be ‘scalable’ and thus should hold to higher masses. In Fig. 10, one would expect such an evolution in a merging system to cause low-luminosity AGNs to lie in the region of low SFRs. Another possibility is that isolated galaxies (which likely make up the bulk of systems shown in Fig. 10) exhibit low SFRs and no AGN activity or low-luminosity AGN activity simply because they lack the strong gravitational torques and shocks, which so efficiently drive gas inflows and fuel high central SFRs and AGN luminosity in gas-rich mergers. The X-ray data in our study are not sensitive to these low-luminosity AGNs, so we cannot directly test their location in Fig. 10.

A more detailed comparison of our quenched fraction results to a wide range of numerical simulations, including hydrodynamical simulations and semi-analytic models is presented in Sherman et al. (2020) as well as a discussion of the physical mechanisms that contribute to galaxy quenching across different environments, stellar masses, and epochs.

7 SUMMARY

We have analysed the relation between AGN and SF activity at $0.5 < z < 3$ by comparing the stellar masses and SFRs of 898 massive galaxies with X-ray luminous AGNs ($L_X > 10^{44} \text{ erg s}^{-1}$) and a large comparison sample of $\sim 320\,000$ galaxies without X-ray luminous AGNs (see Fig. 1 and Table 1). Our samples are selected from a large (11.8 deg^2) area in Stripe82 that has multiwavelength

(X-ray to far-IR) data and corresponds to a very large comoving volume ($\sim 0.3 \text{ Gpc}^3$) at $0.5 < z < 3$, thus minimizing the effects of cosmic variance and captures a large number of rare massive galaxies ($\sim 30\,000$ galaxies with $M_* > 10^{11} M_\odot$) and X-ray luminous AGNs. While many galaxy evolution studies discard the hosts of X-ray luminous AGNs due to the inability of common SED fitting codes to handle such systems, a strength of our study is that we fit the SED of both galaxies with and without X-ray luminous AGN hosts with the CIGALE SED fitting code, which includes AGN emission templates. We summarize our findings below:

(i) The stellar mass and SFRs of galaxies with X-ray luminous AGNs are likely to be overestimated if AGN emission is not included in the SED fit (Fig. 3). For galaxies with large AGN fraction contamination ($f_{\text{AGN}} > 0.4$), the stellar mass can be overestimated by factor of up to 5, on average, while SFRs can be overestimated by a factor of up to 10, on average, if AGN emission templates are not included in the SED fit (Fig. 4).

(ii) The stellar mass function of galaxies with X-ray luminous AGNs (Fig. 5) shows that the number density of galaxies with X-ray luminous AGNs is two to three orders of magnitude lower than galaxies without X-ray luminous AGNs for stellar masses in the range of 10^{10} to $3 \times 10^{11} M_\odot$ at redshifts of $0.5 < z < 3$. This suggests that X-ray luminous AGNs are a rare and rapid phase in galaxy evolution.

(iii) We find that the average SFR of galaxies with X-ray luminous AGNs is higher by a factor of ~ 3 – 10 compared to galaxies without X-ray luminous AGNs at a given stellar mass and redshift (Figs 10 and 11). We remind the reader that these results only hold for X-ray luminous AGNs with X-ray luminosities above the 80 per cent completeness limit at each redshift bin ($L_X > 10^{44.03}$, $10^{44.47}$, $10^{44.78}$, and $10^{45.21} \text{ erg s}^{-1}$, respectively, at $z = 0.5$ – 1.0 , $z = 1.0$ – 1.5 , $z = 1.5$ – 2.0 , and $z = 2.0$ – 3.0). These results are consistent with a scenario where the high SFR and high AGN luminosity are produced by processes that produce large gas inflow rates both into the regions (on scales of a few hundred pc to few kpc) typically associated with high SFRs, as well as the sub-pc region associated with the AGN accretion disc. Examples of processes that drive large gas inflow rates through gravitational torques, tidal torques, and dissipative shocks include gas-rich major mergers, gas-rich minor mergers, and strong tidal interactions in gas-rich systems. It should be noted that in order to drive gas from kpc scales down to the scales of the AGN accretion disc, we need mechanisms that effectively reduce the angular momentum of the gas by several orders of magnitude.

(iv) Due to the unprecedented size of our sample of massive galaxies, we are able to perform one of the first robust explorations of how the quenched fraction of galaxies varies with stellar mass in each redshift bin. The quenched fraction, based on both definitions of quiescence (galaxies with $s\text{SFR} < 10^{-11} \text{ yr}^{-1}$ or galaxies with SFR at least 1 dex below the main sequence) rises with galaxy stellar mass over the range $10^{10} M_\odot$ to about $3 \times 10^{11} M_\odot$ in each of our four redshift bins in the range $0.5 < z < 3$. The vast majority (> 95 per cent) of galaxies with X-ray luminous AGNs at $z = 0.5$ – 3 do not show quenched SF: this suggests that if AGN feedback quenches SF, the associated quenching process takes a significant time to act and the quenched phase sets in after the highly luminous phases of AGN activity.

ACKNOWLEDGEMENTS

JF, SJ, and SS gratefully acknowledge support from the University of Texas at Austin, as well as National Science Foundation grants

AST-1413652 and AST-1757983. JF, SJ, SS, and SLF acknowledge support from National Science Foundation grant AST-1614798. JF acknowledges support from the National Science Foundation Graduate Research Fellowship Program grant DGE-1610403. The authors wish to thank Pedro Capelo for useful comments. The authors acknowledge the Texas Advanced Computing Center (TACC) at The University of Texas at Austin for providing High-Performance Computing (HPC) resources that have contributed to the research results reported within this paper. URL: <http://www.tacc.utexas.edu>.

The Institution for Gravitation and the Cosmos is supported by the Eberly College of Science and the Office of the Senior Vice President for Research at the Pennsylvania State University.

DATA AVAILABILITY

The data underlying this work will be shared upon reasonable request to the corresponding author. Email: jflorez06@utexas.edu

REFERENCES

- Acquaviva V., Gawiser E., Guaita L., 2011, *ApJ*, 737, 47
 Ananna T. T. et al., 2017, *ApJ*, 850, 66 (A17)
 Ananna T. T. et al., 2019, *ApJ*, 871, 240
 Babić A., Miller L., Jarvis M. J., Turner T. J., Alexander D. M., Croom S. M., 2007, *A&A*, 474, 755
 Baldry I. K. et al., 2012, *MNRAS*, 421, 621
 Berta S. et al., 2013, *A&A*, 551, A100
 Bertin E., Arnouts S., 1996, *A&AS*, 117, 393
 Bieri R., Dubois Y., Rosdahl J., Wagner A., Silk J., Mamon G. A., 2017, *MNRAS*, 464, 1854
 Bongiorno A. et al., 2016, *A&A*, 588, A78
 Boquien M., Burgarella D., Roehlly Y., Buat V., Ciesla L., Corre D., Inoue A. K., Salas H., 2019, *A&A*, 622, A103
 Boselli A., Boissier S., Cortese L., Gil de Paz A., Seibert M., Madore B. F., Buat V., Martin D. C., 2006, *ApJ*, 651, 811
 Brammer G. B., van Dokkum P. G., Coppi P., 2008, *ApJ*, 686, 1503
 Brandt W. N., Alexander D. M., 2015, *A&AR*, 23, 1
 Brandt W. N., Hasinger G., 2005, *ARA&A*, 43, 827
 Brennan R. et al., 2015, *MNRAS*, 451, 2933
 Brusa M. et al., 2010, *ApJ*, 716, 348
 Bruzual G., Charlot S., 2003, *MNRAS*, 344, 1000
 Buat V. et al., 2014, *A&A*, 561, A39
 Burlon D., Ajello M., Greiner J., Comastri A., Merloni A., Gehrels N., 2011, *ApJ*, 728, 58
 Calistro Rivera G., Lusso E., Hennawi J. F., Hogg D. W., 2016, *ApJ*, 833, 98
 Calzetti D., Armus L., Bohlin R. C., Kinney A. L., Koornneef J., Storchi-Bergmann T., 2000, *ApJ*, 533, 682
 Capelo P. R., Dotti M., 2017, *MNRAS*, 465, 2643
 Capelo P. R., Volonteri M., Dotti M., Bellovary J. M., Mayer L., Governato F., 2015, *MNRAS*, 447, 2123
 Cattaneo A. et al., 2009, *Nature*, 460, 213
 Chabrier G., 2003, *PASP*, 115, 763
 Choi E., Ostriker J. P., Naab T., Oser L., Moster B. P., 2015, *MNRAS*, 449, 4105
 Ciesla L., Elbaz D., Fensch J., 2017, *A&A*, 608, A41
 Ciesla L., Elbaz D., Schreiber C., Daddi E., Wang T., 2018, *A&A*, 615, A61
 Ciesla L. et al., 2015, *A&A*, 576, A10
 Ciesla L. et al., 2016, *A&A*, 585, A43
 Conroy C., Gunn J. E., White M., 2009, *ApJ*, 699, 486
 Conroy C., Wechsler R. H., 2009, *ApJ*, 696, 620
 Cox T. J., Jonsson P., Somerville R. S., Primack J. R., Dekel A., 2008, *MNRAS*, 384, 386
 da Cunha E., Charlot S., Elbaz D., 2008, *MNRAS*, 388, 1595
 Daddi E. et al., 2007, *ApJ*, 670, 156
 Dale D. A., Helou G., Magdis G. E., Armus L., Díaz-Santos T., Shi Y., 2014, *ApJ*, 784, 83

- Davidzon I. et al., 2013, *A&A*, 558, A23
- Davé R., Anglés-Alcázar D., Narayanan D., Li Q., Rafieferantsoa M. H., Appleby S., 2019, *MNRAS*, 486, 2827
- Delvecchio I. et al., 2014, *MNRAS*, 439, 2736
- Dickinson M., Papovich C., Ferguson H. C., Budavári T., 2003, *ApJ*, 587, 25
- Di Matteo T., Colberg J., Springel V., Hernquist L., Sijacki D., 2008, *ApJ*, 676, 33
- Donnari M. et al., 2019, *MNRAS*, 485, 4817
- Draine B. T., Li A., 2007, *ApJ*, 657, 810
- Elbaz D. et al., 2007, *A&A*, 468, 33
- Elmegreen B. G., 1994, *ApJ*, 425, L73
- Fabian A. C., 2012, *ARA&A*, 50, 455
- Fang J. J. et al., 2018, *ApJ*, 858, 100
- Feltre A., Hatziminaoglou E., Fritz J., Franceschini A., 2012, *MNRAS*, 426, 120
- Ferrarese L., Merritt D., 2000, *ApJ*, 539, L9
- Fliri J., Trujillo I., 2016, *MNRAS*, 456, 1359
- Fontanot F., De Lucia G., Monaco P., Somerville R. S., Santini P., 2009, *MNRAS*, 397, 1776
- Fritz J., Franceschini A., Hatziminaoglou E., 2006, *MNRAS*, 366, 767
- Fumagalli M., Gavazzi G., Scaramella R., Franzetti P., 2011, *A&A*, 528, A46
- Geach J. E. et al., 2017, *ApJS*, 231, 7
- Gebhardt K. et al., 2000, *ApJ*, 539, L13
- Glazebrook K. et al., 2017, *Nature*, 544, 71
- Grogin N. A. et al., 2011, *ApJS*, 197, 35
- Hambrick D. C., Ostriker J. P., Naab T., Johansson P. H., 2011, *ApJ*, 738, 16
- Hao C.-N., Kennicutt R. C., Johnson B. D., Calzetti D., Dale D. A., Moustakas J., 2011, *ApJ*, 741, 124
- Heckman T. M., Best P. N., 2014, *ARA&A*, 52, 589
- Hill G. J., HETDEX Consortium, 2016, HETDEX and VIRUS: Panoramic Integral Field Spectroscopy with 35k Fibers. Astronomical Society of the Pacific Conference Series, San Francisco, California, USA, p. 393
- Hopkins P. F., Hernquist L., Cox T. J., Kereš D., 2008, *ApJS*, 175, 356
- Hopkins P. F., Richards G. T., Hernquist L., 2007, *ApJ*, 654, 731
- Hopkins P. F., Torrey P., Faucher-Giguère C.-A., Quataert E., Murray N., 2016, *MNRAS*, 458, 816
- Hunt L. K., Malkan M. A., 1999, *ApJ*, 516, 660
- Ibar E., Lira P., 2007, *A&A*, 466, 531
- Ilbert O. et al., 2013, *A&A*, 556, A55
- Jahnke K., Macciò A. V., 2011, *ApJ*, 734, 92
- Jogee S., 2006, in Alloin D., ed., Lecture Notes in Physics, Vol. 693, Physics of Active Galactic Nuclei at all Scales. Springer-Verlag, Berlin, p. 143
- Jogee S., Scoville N., Kenney J. D. P., 2005, *ApJ*, 630, 837
- Jogee S. et al., 2009, *ApJ*, 697, 1971
- Kawinwanichakij L. et al., 2020, *ApJ*, 892, 7
- Kirkpatrick A., Sharon C., Keller E., Pope A., 2019b, *ApJ*, 879, 41
- Kirkpatrick A. et al., 2019a, *ApJ*, submitted ([arXiv:1908.04795](https://arxiv.org/abs/1908.04795))
- Knapen J. H., Beckman J. E., Heller C. H., Shlosman I., de Jong R. S., 1995, *ApJ*, 454, 623
- Koekemoer A. M. et al., 2011, *ApJS*, 197, 36
- Kormendy J., Ho L. C., 2013, *ARA&A*, 51, 511
- Kriek M. et al., 2006, *ApJ*, 649, L71
- Kroupa P., 2001, *MNRAS*, 322, 231
- LaMassa S. M., Georgakakis A., Vivek M., Salvato M., Ananna T. T., Urry C. M., MacLeod C., Ross N., 2019, *ApJ*, 876, 50 (LM19)
- LaMassa S. M. et al., 2013a, *MNRAS*, 432, 1351
- LaMassa S. M. et al., 2013b, *MNRAS*, 436, 3581
- LaMassa S. M. et al., 2016, *ApJ*, 817, 172
- Lang D., Hogg D. W., Mykytyn D., 2016, Astrophysics Source Code Library, record ascl:1604.008
- Lehmer B. D. et al., 2008, *ApJ*, 681, 1163
- Leslie S. K., Kewley L. J., Sanders D. B., Lee N., 2016, *MNRAS*, 455, L82
- Liu Z. et al., 2016, *MNRAS*, 459, 1602
- Lusso E. et al., 2012, *MNRAS*, 425, 623
- Madau P., Dickinson M., 2014, *ARA&A*, 52, 415
- Magorrian J. et al., 1998, *AJ*, 115, 2285
- Mahoro A., Pović M., Nkundabakura P., 2017, *MNRAS*, 471, 3226
- Masoura V. A., Mountrichas G., Georgantopoulos I., Ruiz A., Magdis G., Plionis M., 2018, *A&A*, 618, A31
- McLure R. J., Dunlop J. S., 2002, *MNRAS*, 331, 795
- McNamara B. R., Nulsen P. E. J., 2007, *ARA&A*, 45, 117
- Meléndez M., Mushotzky R. F., Shimizu T. T., Barger A. J., Cowie L. L., 2014, *ApJ*, 794, 152
- Moustakas J. et al., 2013, *ApJ*, 767, 50
- Mullaney J. R., Alexander D. M., Goulding A. D., Hickox R. C., 2011, *MNRAS*, 414, 1082
- Muzzin A. et al., 2013, *ApJ*, 777, 18
- Naab T., Ostriker J. P., 2017, *ARA&A*, 55, 59
- Naiman J. P. et al., 2018, *MNRAS*, 477, 1206
- Negri A., Volonteri M., 2017, *MNRAS*, 467, 3475
- Nelson D. et al., 2018, *MNRAS*, 475, 624
- Neškova M., Sirocky M. M., Ivezić Ž., Elitzur M., 2008, *ApJ*, 685, 147
- Noll S., Burgarella D., Giovannoli E., Buat V., Marcillac D., Muñoz-Mateos J. C., 2009, *A&A*, 507, 1793
- Papovich C. et al., 2016, *ApJS*, 224, 28
- Park J., Smith R., Yi S. K., 2017, *ApJ*, 845, 128
- Peterson J. R., Fabian A. C., 2006, *Phys. Rep.*, 427, 1
- Powell M. C., Urry C. M., Cappelluti N., Johnson J. T., LaMassa S. M., Ananna T. T., Kollmann K. E., 2020, *ApJ*, 891, 41
- Pozzetti L. et al., 2010, *A&A*, 523, A13
- Rigby E. E., Best P. N., Brookes M. H., Peacock J. A., Dunlop J. S., Röttgering H. J. A., Wall J. V., Ker L., 2011, *MNRAS*, 416, 1900
- Roos O., Juneau S., Bournaud F., Gabor J. M., 2015, *ApJ*, 800, 19
- Rosario D. J. et al., 2013, *ApJ*, 771, 63
- Sanders D. B., Soifer B. T., Elias J. H., Madore B. F., Matthews K., Neugebauer G., Scoville N. Z., 1988, *ApJ*, 325, 74
- Santini P. et al., 2012, *A&A*, 540, A109
- Schmidt M., 1968, *ApJ*, 151, 393
- Schreiber C. et al., 2015, *A&A*, 575, A74
- Sherman S., et al., 2020, *MNRAS*, submitted
- Sherman S. et al., 2020, *MNRAS*, 491, 3318
- Shimizu T. T., Mushotzky R. F., Meléndez M., Koss M., Rosario D. J., 2015, *MNRAS*, 452, 1841
- Shimizu T. T., Mushotzky R. F., Meléndez M., Koss M. J., Barger A. J., Cowie L. L., 2017, *MNRAS*, 466, 3161
- Somerville R. S., Davé R., 2015, *ARA&A*, 53, 51
- Somerville R. S., Hopkins P. F., Cox T. J., Robertson B. E., Hernquist L., 2008, *MNRAS*, 391, 481
- Speagle J. S., Steinhardt C. L., Capak P. L., Silverman J. D., 2014, *ApJS*, 214, 15
- Springel V., Di Matteo T., Hernquist L., 2005, *MNRAS*, 361, 776
- Springel V. et al., 2018, *MNRAS*, 475, 676
- Stefanon M., Marchesini D., Rudnick G. H., Brammer G. B., Whitaker K. E., 2013, *ApJ*, 768, 92
- Stevens M., et al., 2020, *ApJ*, submitted
- Strüder L. et al., 2001, *A&A*, 365, L18
- Sutherland W., Saunders W., 1992, *MNRAS*, 259, 413
- Timlin J. D. et al., 2016, *ApJS*, 225, 1
- Tristram K. R. W. et al., 2007, *A&A*, 474, 837
- van Dokkum P. G. et al., 2009, *PASP*, 121, 2
- Viero M. P. et al., 2014, *ApJS*, 210, 22
- Vogelsberger M., Genel S., Sijacki D., Torrey P., Springel V., Hernquist L., 2013, *MNRAS*, 436, 3031
- Wellons S. et al., 2015, *MNRAS*, 449, 361
- Whitaker K. E. et al., 2011, *ApJ*, 735, 86
- Whitaker K. E. et al., 2014, *ApJ*, 795, 104
- White S. D. M., Rees M. J., 1978, *MNRAS*, 183, 341
- Wilkins S. M., Trentham N., Hopkins A. M., 2008, *MNRAS*, 385, 687
- Wold I. G. B. et al., 2019, *ApJS*, 240, 5
- Wright E. L. et al., 2010, *AJ*, 140, 1868
- Wuyts S. et al., 2007, *ApJ*, 655, 51
- Yang G., Brandt W. N., Alexander D. M., Chen C.-T. J., Ni Q., Vito F., Zhu F.-F., 2019, *MNRAS*, 485, 3721
- Yang G. et al., 2017, *ApJ*, 842, 72

APPENDIX A: ASSESSING THE IMPACT OF WISE DATA ON THE ANALYSIS

Fig. 1 and Table 1 show that if we require WISE detection, our sample of galaxies with X-ray luminous AGNs would be reduced from 932 sources (in sample S1-Lum-AGN) to 356 sources (in sample S1-Lum-AGN-WISE), while our sample of galaxies without X-ray luminous AGNs be reduced from 318 904 sources (in sample S2-No-Lum-AGN) to 4695 sources (in sample S2-No-Lum-AGN-WISE). In order to better sample the X-ray luminosity function and prevent a drastic reduction in sample size, we use the samples without WISE data (S1-Lum-AGN and S2-No-Lum-AGNs) in our main analysis. However, here in the Appendix, we perform some tests where we compare the SFR and stellar mass derived with and without WISE mid-IR data, and demonstrate that the inclusion of WISE data would not change the results of this work.

In Fig. A1, we show the results of a test similar to that shown in Fig. 4 for galaxies with X-ray luminous AGNs and with a WISE detection. We find that when WISE photometry is included in the SED fitting, our results remain largely the same for this test. That is, we still find that stellar masses and SFRs can be overestimated, on

average, by a factor of up to ~ 5 and ~ 10 for $f_{\text{AGN}} > 0.4$, respectively, if AGN emission templates are not included in the SED fit.

The top panels of Fig. A2 show the stellar mass estimate using WISE data in the SED fit versus the stellar mass estimate without using WISE data for galaxies with and without X-ray luminous AGNs. The bottom panels of Fig. A2 show the SFR estimate using WISE data in the SED fit versus the SFR estimate without using WISE data for both samples of galaxies with and without X-ray luminous AGNs. The stellar mass estimates do not change by much when WISE data are added to the SED fit. The SFR estimates, however, change by quite a bit on a case to case basis and have a large scatter of ~ 0.3 dex. There is no systematic offset, however, in SFRs derived with and without WISE data.

In Fig. A3, we show the mean SFR of galaxies with (S1-Lum-AGN-WISE) and without X-ray luminous AGNs (S2-No-Lum-AGN-WISE) and with photometry out to $22\ \mu\text{m}$. Although we have poor number statistics, we find that the trends are consistent with the trends we see in Fig. 11 for both samples of galaxies with and without X-ray luminous AGNs as the sample of galaxies with X-ray luminous AGNs has higher SFRs, on average, at a given stellar mass.

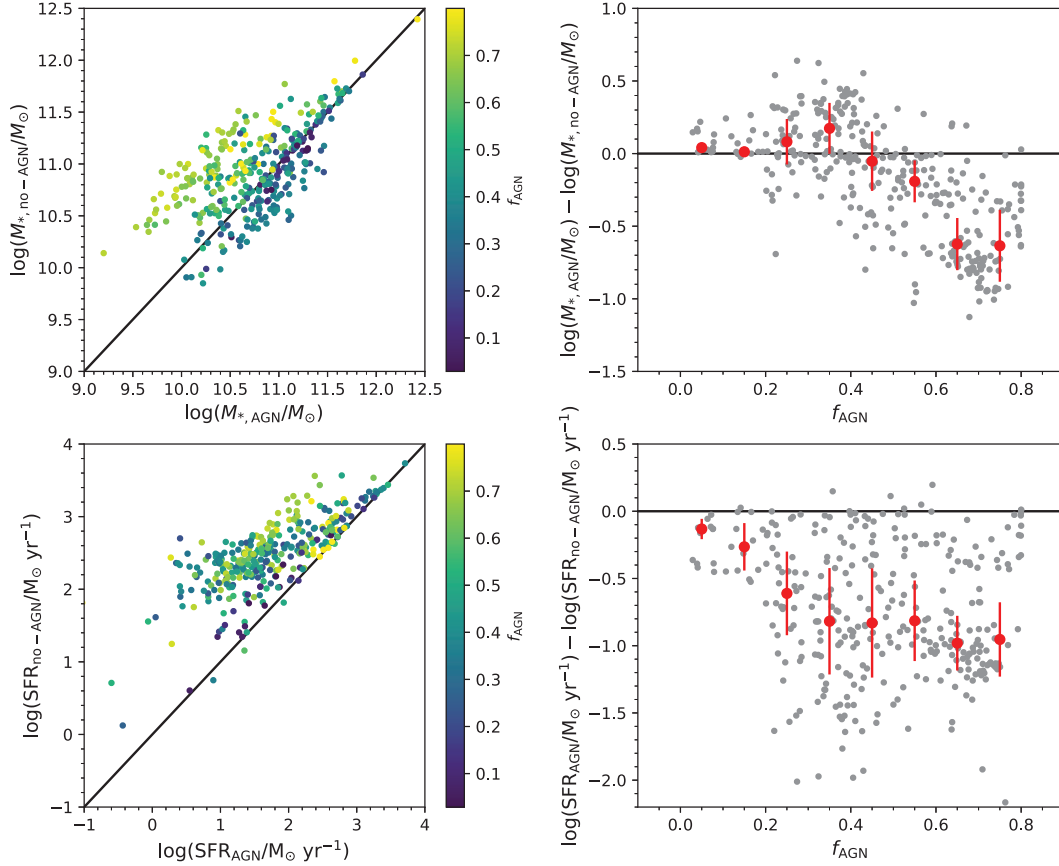


Figure A1. Similar to Fig. 4 but for sources in S1-Lum-AGN-WISE, that is, galaxies with X-ray luminous AGNs and WISE photometry available. Left: Stellar mass and SFR estimates for our sample of galaxies with X-ray luminous AGNs (S1-Lum-AGN-WISE) when AGN emission is included in the SED fit (x -axis) versus when AGN emission is not included (y -axis). Points are coloured according to their fractional AGN contamination (f_{AGN}), defined as the fraction of light in the 8–1000 μm wavelength range that is contributed by the AGN. Right: Difference in log stellar mass and SFR as a function of the fractional AGN contamination. Also shown is the median (red circles) log difference of stellar mass and SFR with and without the AGN emission in the SED fit in four bins of f_{AGN} with the median absolute deviation shown as error bars. We note that the results of this test are qualitatively similar to those shown in Fig. 4, where WISE photometry is not used in the sample.

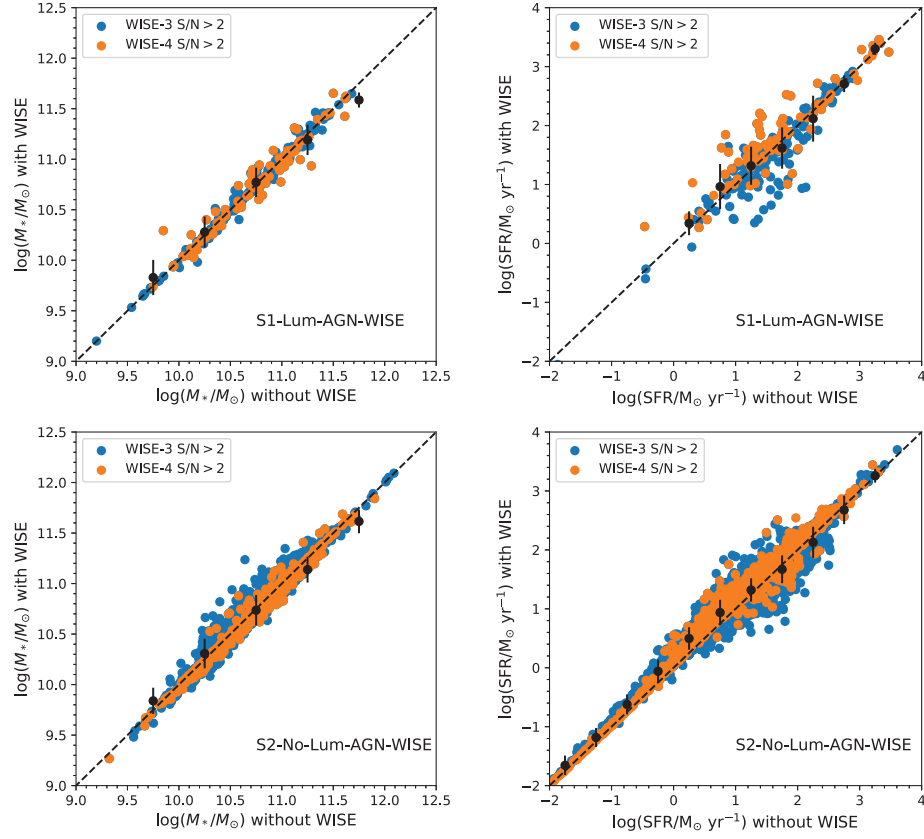


Figure A2. Left: The stellar mass estimate of galaxies with (S1-Lum-AGN-WISE, top) and without (S2-No-Lum-AGN, bottom) X-ray luminous AGNs. Right: The SFR estimate of galaxies with (S1-Lum-AGN-WISE, top) and without (S2-No-Lum-AGN, bottom) X-ray luminous AGNs. The y-axis on all panels shows the stellar mass (or SFR) value obtained when WISE-3 or WISE-4 photometry is included in the SED fit, while the x-axis shows the value that is obtained when WISE photometry is not included in the SED fit. We find that stellar masses do not vary by more than 0.5 dex when WISE data is excluded from the photometry in either sample. SFRs, on the other hand, can vary by a factor of ~ 1 dex when WISE photometry is not included in the SED fit, however, we find no systematic bias.

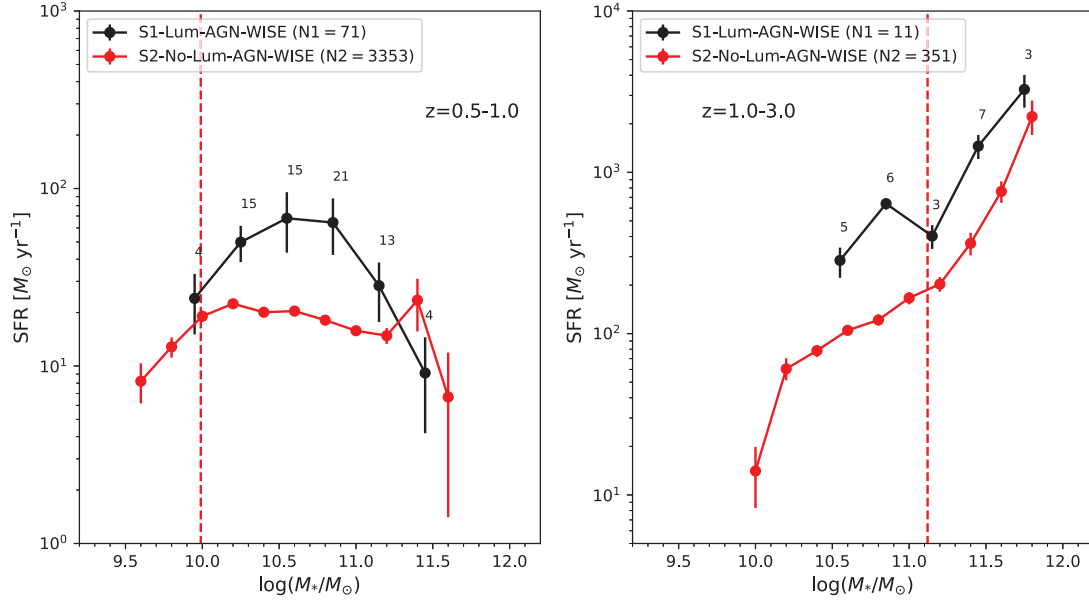


Figure A3. The mean SFR of galaxies with (S1-Lum-AGN-WISE) and without (S2-No-Lum-AGN-WISE) X-ray luminous AGNs as a function of stellar mass in two different bins of redshift. The dashed vertical line shows the mass completeness limit discussed in Section 4.1. Our results here for the two samples with WISE photometry do not change qualitatively from those of Fig. 11.

This paper has been typeset from a \LaTeX file prepared by the author.